INSTITUTE OF PHYSICS PUBLISHING REPORTS ON PROGRESS IN PHYSICS

Rep. Prog. Phys. **69** (2006) 759–796 doi:10.1088/0034-4885/69/3/R05

Time-dependent single-electron transport through quantum dots

Toshimasa Fujisawa[1,2], **Toshiaki Hayashi**[1] **and Satoshi Sasaki**[1]

[1] NTT Basic Research Laboratories, NTT Corporation 3-1 Morinosato-Wakamiya, Atsugi 243-0198, Japan
[2] Tokyo Institute of Technology, 2-12-1, Ookayama, Meguro, Tokyo 152-8550, Japan

Received 21 November 2005, in final form 16 January 2006
Published 20 February 2006
Online at stacks.iop.org/RoPP/69/759

Abstract

We describe time-dependent single-electron transport through quantum dots in the Coulomb blockade regime. Coherent dynamics of a single charge qubit in a double quantum dot is discussed with full one-qubit manipulation. Strength of decoherence is controlled with the applied voltage, but uncontrolled decoherence arises from electron–phonon coupling and background fluctuations. Then energy-relaxation dynamics is discussed for orbital and spin degree of freedom in a quantum dot. The electron–phonon interaction and spin–orbit coupling can be investigated as the dissipation problem. Finally, charge detection measurement is presented for statistical analysis of single-electron tunnelling transitions and for a sensitive qubit read-out device.

(Some figures in this article are in colour only in the electronic version)

Contents

1. Introduction

Time-dependent phenomena in nanostructures are of growing interest for understanding and controlling their dynamic behaviour. One of the applications is quantum computing, in which some kinds of information processing can be performed *efficiently* in a parallel fashion by manipulating particles (qubits) in a programmable manner [1,2]. Various quantum algorithms have been successfully demonstrated in some physical systems [3], and there has been progress in integrating large number of qubits required for practical quantum computers, especially in solid state systems [4–9]. Although the realization of a practical quantum computer may require enormous research activity, quantum information research has already succeeded in the sense that a common language is provided for communicating with interdisciplinary researchers. Quantum dynamics can now be discussed in terms of quantum information theory, which indeed facilitates discussions between physicists, chemists, mathematicians and quantum engineers.

Generally, any quantum process that changes an initial state (density operator) to a final state can be described by a completely-positive trace-preserving mapping [1]. Knowledge of the mapping suffices for defining a quantum information process. Identical mapping provides the same process regardless of the microscopic origin of the interactions. Quantum computation is based on an assembly of unitary operations, which can be decomposed into some fundamental unitary operations on one- or two- qubit subsystems. Therefore, the problem can be reduced to a few kinds of unitary operators. Actually, realistic operations are influenced and degraded by the environment coupled to the qubit system, and thus the mapping becomes a non-unitary quantum process [10]. Two important quantum processes that degrade the coherence of the system are dissipation, in which the energy of the quantum system is exchanged with the environment, and dephasing, in which the phase of the quantum system is randomized by the environment. The former is often characterized by longitudinal relaxation time (T_1), and the latter by transverse relaxation time (T_2). In addition, the measurement process can also be considered a quantum process under coupling to the measurement apparatus. Quantum computing requires a full set of quantum processes for initializing all qubits, performing one- and two-qubit unitary operations, measuring each qubit state and avoiding errors from non-unitary operations [11].

Quantum dynamics in nanometre-scale solid-state devices is attractive for controlling some single quanta in a tailored structure with a programmable sequence of quantum processes. Superconducting circuits with Josephson junctions have successfully demonstrated one and two-qubit operations with a high degree of coherency [12,13]. The system can be well isolated from the environment by designing device parameters and a proper pulse sequence. Another system is the semiconductor quantum dot (QD), which provides artificial electronic states that can be controlled with external voltages. Since atomic-like electronic states can be designed and actually formed in a semiconductor device, QDs are often referred to as artificial atoms [14–17]. High controllability of electronic states is useful for studying the dynamic behaviour of artificial quantum systems as well as that of quantum computing systems. There are two major choices of the qubit bases: the spin degree of freedom in a single QD and the charge (orbital) degree of freedom in a double quantum dot (DQD). In this paper, we shall review some research on spin and charge qubits in QDs in connection to quantum information processing and physical phenomena underlying realistic devices.

1.1. Charge qubit in a DQD

A single-electron charge qubit can be defined in a DQD, in which one electron occupies the ground state of one dot or the other [18]. There are two types of coupling between the

two QDs: electrostatic coupling, which prevents two electrons occupying the same QD; and tunnelling, which allows an electron to occupy two QDs [19]. This allows us to describe the DQD with a simplified two-level system. One-qubit unitary operation has been demonstrated with Larmor precession, as will be shown in section 2.3 [20, 21]. Two-qubit unitary operation can be designed with dipole coupling between neighbouring charge qubits (section 2.5) [22]. Controlled-NOT (CNOT) gate operation and entanglement state have been proposed and discussed theoretically for different geometries of DQD arrays [23]. The charge state can be read out with a sensitive charge detector, such as a single electron transistor (SET) or a quantum point contact (PC) device, which will be discussed in section 4.3. A charge qubit is advantageous for all-electric control with state-of-the-art high-speed electronics for programmable pulse sequences. Actually, superconducting charge qubits have been used for the successful demonstration of CNOT operation [24] as well as single-shot measurement [25]. Therefore, similar measurements are also expected for semiconductor QD systems.

However, decoherence is a serious problem as described in section 2.4. Most single-electron devices suffer from background charge fluctuations, in which electron occupation of impurities in the device is thermally activated [26]. Although the thermally activated noise should decrease with decreasing temperature, the noise can also be excited during qubit operation even at zero temperature [25]. Background charge fluctuation has $1/f$ frequency dependence, and its low-frequency part randomizes the phase of the qubit (decoherence). Echo techniques developed in magnetic spin resonance experiments are useful in recovering the coherency of the system [12]. However, the high-frequency part of the fluctuation cannot be safely neglected and gives rise to significant decoherence and dissipation [25]. Understanding and eliminating the fluctuation will require much effort in device fabrication. Electron–phonon interaction is another decoherence source important to semiconductor systems. Piezoelectric coupling, which appears in polar materials such as GaAs, is dominant for low-energy excitations and brings about super-Ohmic coupling to qubit systems [27, 28]. Actually, resonant tunnelling current through a DQD has revealed a spectral function of electron–phonon coupling [29].

1.2. Electron spin qubit

Electron spin is a natural two-level system and thus ideal for a qubit [30–32]. An electron confined in a QD is a convenient way to handle individual electron spins. According to Loss and DiVincenzo [31], unitary operation of a single spin can be performed by Rabi oscillation with oscillating magnetic field at the electron spin resonance (ESR) condition. Arbitrary unitary operation for one qubit can be designed using two kinds of ESR oscillations, for instance, with a different phase of the oscillating field. Two-qubit operation can be performed by applying voltage-controlled exchange interaction between electrons in neighbouring QDs [32]. The two-electron wavefunction with the spin singlet and triplet configurations experiences different Coulomb repulsion, resulting in energy splitting between the singlet and triplet states [33]. The opening of this splitting for a short period can be used to swap the spin information of the two-electron system (swap operation). The combination of the swap operation and one-qubit operation generates an arbitrary unitary operation including CNOT gate and more complicated operations.

Much experimental progress has been made in this direction. Zeeman splitting, which determines the Larmor precession frequency, has been measured with spin-dependent transport through the spin-up or spin-down branch of single-electron state in a QD [34, 35]. Such spin-dependent tunnelling under large Zeeman splitting can be used to prepare an initial state in the ground state. A spin-up electron (ground state for GaAs) can be selectively injected into

a QD. One can also determine the spin state of a QD using spin-dependent tunnelling, in which only a spin-down electron with higher energy is allowed to escape from the QD [36]. High-speed charge detection determines whether the electron has escaped or remains; thus single-electron spin state can be determined (section 4.3). This single-shot read out technique is quite important for the statistical analysis of the multiple-qubit system and essential for studying correlation in an entanglement state.

In contrast to an electron in a vacuum, the electron g-factor largely deviates from 2 because of spin–orbit coupling in a compound semiconductor (e.g. −0.44 for bulk GaAs) [37]. Despite large spin–orbit coupling, electron spin in a QD is expected to have a relatively long relaxation time [38, 39]. Actually, the dissipation time (T_1) of an electron spin can be made longer than 1 ms, which is about 10^7 times longer than the typical spin precession time [36, 40, 41], as discussed in section 3.3. However, decoherence time (T_2) is strongly affected by the magnetic field fluctuation caused by nuclear spin fluctuation. The ESR signal of conduction electrons in GaAs shows significant broadening and hysteresis due to hyperfine coupling to the nuclear spins of the host material, implying T_2 of about 10 ns as estimated from the width of the ESR peak. Recent spin-dependent transport experiments indicate that the nuclear spin fluctuation gives rise to a fluctuation in the local magnetic field, resulting in a short dephasing time of about 10 ns [42].

For coherent control of an electron spin qubit, ESR has been demonstrated for an isolated electron trapped in a defect in silicon [43]. This technique could be applied for one-qubit manipulation. However, ESR Rabi oscillation would remain relatively slow when the experimentally available magnetic field is considered. Other techniques, such as the voltage-controlled spin–orbit coupling effect, can be very efficient for spin manipulation in semiconductors [44]. Two-electron exchange splitting for two-qubit operation has been extensively studied in DQDs. In contrast to the relatively large exchange energy in a single QD [45], the exchange spitting of spatially separated electrons in a DQD can be too small to resolve in the conventional transport measurement [33, 46]. Extremely small exchange splitting can be measured with the aid of hyperfine coupling to nuclei. Recently, coherent oscillations between spin singlet and triplet states have been successfully demonstrated with voltage-controlled exchange splitting [47]. Significant decoherence from the nuclear spin fluctuation can be removed by using an echo technique to cancel the low-frequency part of the fluctuations. Nevertheless, for the control of individual spins, controlling nuclear spins may be required in order to improve the spin relaxation time. The nuclear spin fluctuation can be minimized at full nuclear-spin polarization. It should be noted that hyperfine coupling may be useful in a positive way in that the electron spin information can be transferred to nuclear spin information, as theoretically predicted in [48].

1.3. Entanglement state

In addition to these standard approaches to quantum computing, there are various techniques that are particularly important for quantum information science. For instance, successful generation of an entangled photon pair relies on a non-linear optical process that generates two visible photons from an ultraviolet photon [2]. Each photon of an entangled pair can be analysed with a polarizing beam splitter and photon detectors. The coincidence statistics of photon detection at various angles indicates a violation of Bell's inequality, which tells us the quantum mechanical nature of a non-local photon pair. The generation of entangled states can be used in various kinds of quantum communication devices, like quantum teleportations and quantum repeaters.

How can we perform such experiments for electrons in QDs? We have to develop an electronic version of each optical component, such as an entanglement generator, polarizing beam splitter/analyser and photon counting device. Various techniques for ballistic electron

optics have been developed since the 1990s. It is known that an electron can travel ballistically for more than 100 μm in a high-mobility semiconductor heterostructure [49,50]. The electron trajectory can be modulated locally by gate electrodes, and tuneable electron refraction in an electron prism as well as controllable reflection for electron mirrors have actually been demonstrated [51]. Electron transport also shows interferometric effects, like the Aharonov–Bohm effect and the Al'tshuler–Aronov–Spivak effect in a ring geometry [52–54]. It has been demonstrated that interference patterns in a double-slit interferometer are degraded by detecting which path (slit) an electron transports through, as quantum mechanics predicts [55]. Furthermore, the two-electron collision noise in an electron beam splitter indicates anti-bunching characteristics of Fermionic symmetry [56]. When the spin degree of freedom is considered, bunching (anti-bunching) is expected for spin singlet (triplet) correlation. These measurements have motivated further studies on electron flying qubits in semiconductors. The charge detection measurement described in section 4 may be useful for developing an electron counting device.

Some theoretical studies have proposed generation and detection schemes for entanglement spin pair in mesoscopic electron transport [57]. Bell-state measurement can be performed with electron interferometers, beam splitters and local spin rotations. The selection rule in the relaxation process may be useful for selecting one of the entanglement states as described in section 3.4. In addition, it has been theoretically predicted that the single-charge measurement is essential for the exponential speedup of quantum computation with electron flying qubits [58].

These quantum information techniques with electron charge and spin can be developed by understanding fundamental electron dynamics in quantum dots. In this paper, we describe some recent progress in time-dependent single-electron transport through quantum dots. In section 2, coherent dynamics of a single charge qubit in a DQD is described. Full one-qubit manipulation with controlled decoherence is demonstrated. Energy relaxation dynamics is discussed in section 3. The electron–phonon interaction and spin–orbit coupling can be investigated as the dissipation problem in QDs. A possible scheme for generating the spin entanglement state is also described. Finally, charge detection measurement is presented in section 4. Statistical analysis of single electron tunnelling transitions is discussed with possible applications for electron counting and a sensitive qubit read-out device.

2. Charge qubit in a DQD

2.1. DC transport characteristics of a DQD

The transport properties of a semiconductor DQD have been studied extensively (for reviews, see [14, 59, 60]). The DQD considered in this section consists of two lateral QDs, which are coupled to each other through a tunnel barrier. Each QD is also connected to an electron reservoir via a tunnel junction, as shown by the equivalent circuit in figure 1(*a*) and the energy diagram in figure 1(*b*). Each tunnel barrier has a small coupling capacitance as well as tunnelling coupling, and single-electron transport through the DQD can be measured. Here, we denote a tunnel coupling between localized states in the two dots as T_c and tunnelling rates for the left and right tunnel barriers as Γ_L and Γ_R, respectively. In addition, the DQD is connected to gate voltages V_l and V_r via capacitors C_l and C_r, respectively, so that the local electrostatic potential of each dot can be controlled independently. The difference of the electrochemical potentials of the two dots is expressed as $\varepsilon = \varepsilon_L - \varepsilon_R$. The energy difference between the electrochemical potentials μ_L and μ_R of the left and right reservoirs corresponds to the applied source–drain voltage V_{sd}.

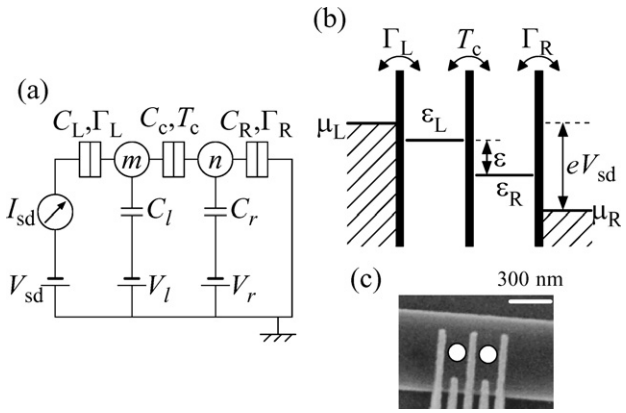

Figure 1. (*a*) Electric circuit model of a DQD containing m and n electrons in the left and right dot, respectively. The two QDs are coupled to each other via a tunnel junction, and each dot is connected to an electron reservoir via a tunnel junction. The electrostatic potential of the left (right) quantum dot is controlled by the gate voltage V_l (V_r) through the capacitance C_l (C_r). (*b*) Energy diagram of a double quantum dot. T_c is a tunnel coupling between the two quantum dots. Γ_L and Γ_R are tunnelling rates for the left and right tunnel barriers. The difference of the electrochemical potentials between the left (μ_L) and right (μ_R) reservoirs corresponds to the source–drain voltage eV_{sd}. The relative position of the electrochemical potential of each quantum dot can be controlled by the gate voltage V_l (V_r). ε is the difference in the electrochemical potentials between the two quantum dots. (*c*) SEM image of a double quantum dot structure.

A DQD can be routinely fabricated using various techniques. High-quality QDs are often fabricated from a two-dimensional electron gas in a GaAs/AlGaAs modulation-doped heterostructure using standard semiconductor fabrication processes, such as electron beam lithography, dry etching and gate metallization [29,61,62]. As shown in the scanning electron micrograph of figure 1(*c*), a narrow conductive channel is formed between the upper and lower etched grooves (dark regions). Three tunnelling barriers are formed by applying negative voltages to the gate electrodes (the bright vertical lines), leaving the left and right QDs (white circles) between the source and drain electrodes. A very simple system where just one electron occupies a DQD can also be made by optimizing the device structure [36].

In these devices, all DQD parameters (T_c, Γ_L, Γ_R, ε and eV_{sd}) can be controlled with external voltages almost independently. The total energy of the system is given by its enthalpy, which is the electrostatic charging energy in all capacitors subtracted by the work that has been done by the voltage sources [59]. The stable charge configuration (m, n) with m electrons in the left QD and n electrons in the right QD is determined to minimize the total energy. A schematic stability diagram of a DQD is depicted in the V_l–V_r plane in figure 2(*a*). When the tunnelling coupling (T_c) is negligibly small, the boundaries of the stable charge states appear as a honeycomb pattern, a part of which is shown by dashed lines. The triple points, E and H, of three charge states are separated by a length corresponding to the inter-dot Coulomb energy U. Electrons pass through three tunnel barriers sequentially in the vicinity of triple points. For example, transport at E is illustrated in figure 2(*b*), where an *electron* travels from the left to the right lead. On the other hand, the tunnelling process at H can be viewed as *hole* transport, as the unoccupied state (hole) moves from the right to the left (not shown in the diagram).

When the tunnelling coupling (T_c) is significantly large, the chemical energy of the DQD has to be considered in describing the stable charge configuration. The charging diagram

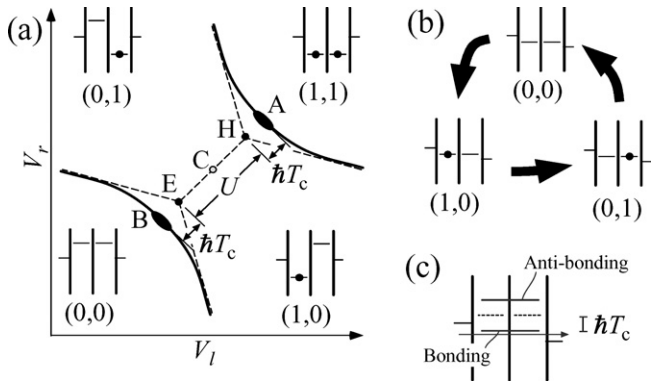

Figure 2. (*a*) Schematic stability diagram of a DQD in a linear transport regime. (m, n) represents a stable charge state of the DQD. U and T_c correspond to the inter-dot Coulomb energy and the tunnel coupling, respectively. (*b*) Sequential electron transport for forward direction at the triple point E. (*c*) Coherent electron transport through the bonding state at B.

deviates from the honeycomb pattern as shown by solid lines in figure 2(*a*). The minimum distance between A and B is increased by the coupling energy $\Delta \equiv 2\hbar T_c$ from its original value U. The ground state on the line between A and B is now a bonding state (superposition) of the (0, 1) and (1, 0) charge states. In this case, linear transport is allowed only on the solid lines close to points A and B. Coherent electron transport through the bonding state is a suitable picture, as shown in figure 2(*c*).

When a large source–drain bias voltage V_{sd} is applied, the conductive regions change from triple points to triangular shaped regions as shown in figure 3(*a*), where the sequential tunnelling regime is considered for simplicity. The electron-like transport around the triple point E is allowed when the electrochemical potential of the left QD is below that of the left reservoir ($\varepsilon_L < \mu_L$ bounded on the lines, l_1), that of the right QD below that of the left one ($\varepsilon_R < \varepsilon_L$ bounded on the lines, l_{res}), and that of the right reservoir below that of the right QD ($\varepsilon_R < E_R$ bounded on the lines, l_4). These conditions determine the lower-left triangle in figure 3(*a*). Similarly, hole-like transport is allowed in the upper-right triangle. These triangles for electron- and hole-transport are separated by the inter-dot Coulomb energy U.

Since the electron energy is quantized in a QD, transport between the dots is allowed basically only for resonant condition ($\varepsilon = \varepsilon_L - \varepsilon_R = 0$), which is indicated by the thick line in figure 3(*a*). The current peak profile is expected to be the Lorentzian form

$$I(\varepsilon) = \frac{e}{\hbar} \frac{\Gamma_R |T_c|^2}{\varepsilon^2 + \Gamma_R^2/4 + |T_c|^2(1 + \Gamma_R/\Gamma_L)}, \tag{1}$$

for electron flow from the left to the right. Figure 3(*b*) shows a typical resonant tunnelling peak fitted with equation (1) [63, 64]. The current spectrum often involves inelastic current at the off-resonant condition as seen on the positive ε side of the traces in figure 3(*b*) and the corresponding grey region in figure 3(*a*). This inelastic current is attributed to electron–phonon coupling, in which the electron can tunnel from a higher-energy state in one dot to a lower-energy state in the other dot by spontaneously emitting an acoustic phonon. This electron–phonon coupling will be discussed with the decoherence problem in section 2.4 and momentum relaxation in section 3.2.

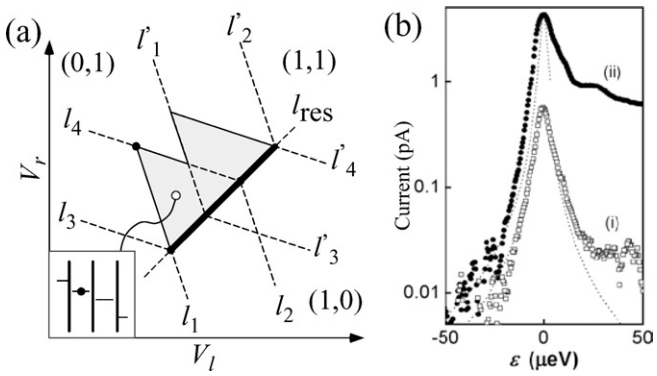

Figure 3. (*a*) A schematic stability diagram of a double quantum dot at a finite bias voltage V_{sd}. Resonant tunnelling current can flow through the device along the bottom thick line of the triangles where the chemical potentials of the two quantum dots are aligned. Inelastic tunnelling current flows inside the grey triangles. (*b*) Typical resonant current. The gate voltages are converted to the energy difference ε. Dashed lines are Lorentzian curves fitted to the data.

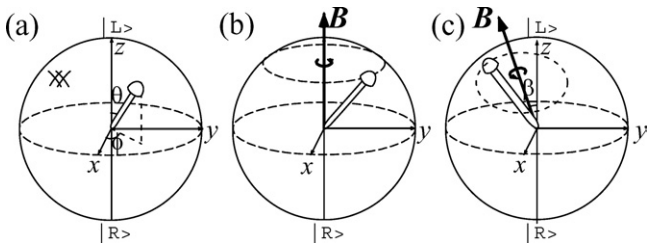

Figure 4. (*a*) Bloch sphere representation of a state of the two-level system. (*b*) Larmor precession of a pseudospin about the effective magnetic field parallel to the z-axis ($\Delta = 0$). (*c*) Larmor precession of a pseudospin about the general effective magnetic field ($\Delta \neq 0$).

2.2. Dynamics of a charge qubit in a DQD

Here, we describe idealized dynamics of a two-level system composed of a single energy level in each dot. The Hamiltonian of a closed system, i.e. an isolated DQD without any reservoirs can be written in the form

$$H_{\mathrm{TLS}} = \varepsilon_{\mathrm{L}}|L\rangle\langle L| + \varepsilon_{\mathrm{R}}|R\rangle\langle R| + T_{\mathrm{c}}(|L\rangle\langle R| + |R\rangle\langle L|), \tag{2}$$

$$= \frac{1}{2}\varepsilon\sigma_z + \frac{1}{2}\Delta\sigma_x + \mathrm{const}, \tag{3}$$

with the same notation defined in figure 1(*b*). σ_x and σ_z are the x and z components of the Pauli matrices, respectively, on the basis of localized states $|L\rangle$ and $|R\rangle$ in the DQD. This can be seen as a spin–1/2 system subjected to an external magnetic field $\boldsymbol{B} = (\Delta, 0, \varepsilon)$: $H = \frac{1}{2}\boldsymbol{\sigma}\cdot\boldsymbol{B}$. Therefore, the mathematical structure of the DQD is the same as that of a spin–1/2 system. An arbitrary state $|\psi\rangle$ in the two-dimensional (one-qubit) Hilbert space can be expressed as

$$|\psi\rangle = \cos\frac{\theta}{2}|L\rangle + \mathrm{e}^{\mathrm{i}\phi}\sin\frac{\theta}{2}|R\rangle, \tag{4}$$

where the coupling angle θ and the phase ϕ can be identified by a point on a sphere, known as Bloch-sphere representation, as shown in figure 4(*a*). The North and South poles correspond to $|L\rangle$ and $|R\rangle$, respectively.

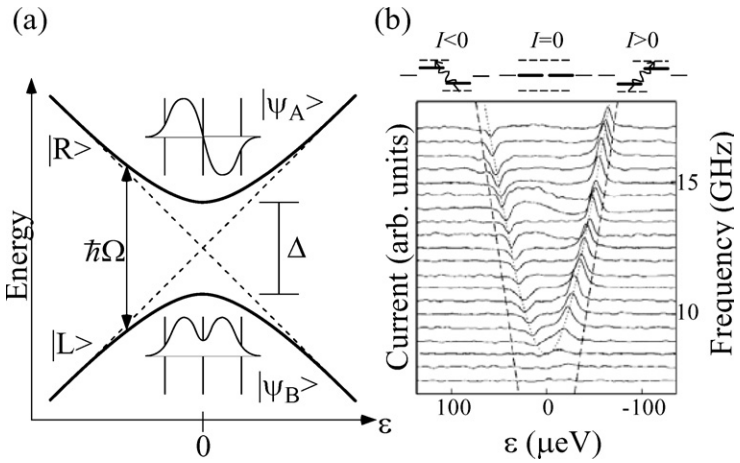

Figure 5. (*a*) Schematic diagram of a two-state system. Dotted lines are the energy levels for $|L\rangle$ and $|R\rangle$. Solid lines are the energy levels for the bonding ($|\psi_B\rangle$) and antibonding ($|\psi_A\rangle$) states. With a finite coupling Δ between $|L\rangle$ and $|R\rangle$, the energy levels of the two states $|\psi_B\rangle$ and $|\psi_A\rangle$ are anticrossed. The gap energy of the anticrossing corresponds to the coupling energy, Δ. (*b*) Photon-assisted tunnelling current spectra. Each line is offset such that the right vertical axis gives the applied frequency. The diagrams show photon-assisted tunnelling between the two QDs.

The eigenstates for the Hamiltonian of equation 2 are the bonding ($|\psi_B\rangle$) and anti-bonding ($|\psi_{AB}\rangle$) states:

$$|\psi_{AB}\rangle = \cos\left(\frac{\beta}{2}\right)|L\rangle + \sin\left(\frac{\beta}{2}\right)|R\rangle, \tag{5}$$

$$|\psi_B\rangle = \sin\left(\frac{\beta}{2}\right)|L\rangle - \cos\left(\frac{\beta}{2}\right)|R\rangle, \tag{6}$$

where $\beta = \arctan(\Delta/\varepsilon)$ is the coupling angle. Any state on the longitudinal circle at $\phi = 0$ can be prepared as eigenstates of the system by adjusting β. The corresponding eigenenergies, $\pm\frac{1}{2}\hbar\Omega = \pm\frac{1}{2}\sqrt{\varepsilon^2 + \Delta^2}$, show anti-crossing behaviour, as shown in figure 5(*a*). With increasing ε ($|\varepsilon| \gg \Delta$), the eigenstates approach the base ket vectors $|L\rangle$ and $|R\rangle$.

This energy splitting has been clearly observed in photon-assisted tunnelling transport measurements on a strongly coupled DQD [65]. Microwave voltage of frequency f applied to a gate electrode modulates the energy bias $\varepsilon = \varepsilon_0 + \varepsilon_1 \cos(2\pi f t)$, which allows transition between the bonding and the anti-bonding state by microwave absorption or emission at the resonant condition, $\Omega = 2\pi f$ [19, 66]. This transition is measured with a current from the source to the drain electrode weakly coupled to the DQD. As shown in figure 5(*b*), the obtained current spectra exhibit a hyperbolic dependence of peak position, which clearly indicates the formation of the bonding and anti-bonding states. It should be noted that microwave spectroscopy probes the coherent coupling only when the microwave excitation causes weak perturbation ($\varepsilon_1 \ll hf$). When an intense microwave field is applied, the system is described by quasi-eigenstates (Floquet state), where an electron and photon are strongly coupled [67]. The resonant condition changes with the microwave amplitude approximately as $\Omega J_0(\varepsilon_1/hf) = 2\pi f$, where $J_n(x)$ is the nth order Bessel function of the first kind. Such dynamic coupling between an electron and photons has actually been demonstrated using microwave spectroscopy [68].

Now, we turn to the coherent dynamics of a DQD in the absence of a microwave field. Suppose non-stationary superposition of eigenstates are prepared by some means, for instance, by changing the system Hamiltonian instantly from one to another, which do not commute with each other. Non-stationary superposition shows Larmor precession about the fictitious magnetic field $\boldsymbol{B}$ under the time-independent Hamiltonian. The time-evolution operator is given by

$$U(t) = \exp\left(\frac{-\mathrm{i}Ht}{\hbar}\right) = \exp\left(\frac{-\mathrm{i}\boldsymbol{\sigma}\cdot\boldsymbol{B}t}{2\hbar}\right). \tag{7}$$

The motion in the Bloch sphere is schematically shown in figure 4(*b*) for the $\Delta = 0$ case and figure 4(*c*) for the general case of $\varepsilon \sim \Delta > 0$. Therefore, any state on the Bloch sphere can be prepared by appropriate Larmor precession. Arbitrary one-qubit operation can be designed by combining two Larmor precessions in, for instance, the Euler angle decomposition, $U_y(\gamma)U_z(\beta)U_y(\alpha)$, with precession operator $U_{y/z}$ along the y/z axis.

In contrast, practical DQDs are often coupled to some electrodes. Consider the situation where both eigenstates are in the source–drain transport window ($\mu_\mathrm{L} > \pm\frac{1}{2}\hbar\Omega > \mu_\mathrm{R}$) under a large energy bias, $\mu_\mathrm{L} - \mu_\mathrm{R} = eV_\mathrm{sd} \gg k_\mathrm{B}T$. We neglect double occupancy where two electrons occupy the DQD. An electron can enter the DQD only from the left electrode at rate Γ_L and can escape only to the right lead at rate Γ_R. These tunnelling processes induce decoherence to the charge qubit in the DQD. The system can be described by a density matrix, ρ, which can be obtained by considering coupling to the electronic states in the electrodes. Under the Born–Markov approximation, master equations for the reduced density matrix read

$$\frac{\mathrm{d}}{\mathrm{d}t}\rho_\mathrm{LL} = -\mathrm{i}\frac{\Delta}{2}(\rho_\mathrm{RL} - \rho_\mathrm{LR}) + \Gamma_\mathrm{L}(1 - \rho_\mathrm{LL} - \rho_\mathrm{RR}), \tag{8}$$

$$\frac{\mathrm{d}}{\mathrm{d}t}\rho_\mathrm{RR} = \mathrm{i}\frac{\Delta}{2}(\rho_\mathrm{RL} - \rho_\mathrm{LR}) - \Gamma_\mathrm{R}\rho_\mathrm{RR}, \tag{9}$$

$$\frac{\mathrm{d}}{\mathrm{d}t}\rho_\mathrm{LR} = -\mathrm{i}\varepsilon\rho_\mathrm{LR} - \mathrm{i}\frac{\Delta}{2}(\rho_\mathrm{RR} - \rho_\mathrm{LL}) - \frac{\Gamma_\mathrm{R}}{2}\rho_\mathrm{LR}, \tag{10}$$

$$\frac{\mathrm{d}}{\mathrm{d}t}\rho_\mathrm{RL} = \mathrm{i}\varepsilon\rho_\mathrm{RL} + \mathrm{i}\frac{\Delta}{2}(\rho_\mathrm{RR} - \rho_\mathrm{LL}) - \frac{\Gamma_\mathrm{R}}{2}\rho_\mathrm{RL}. \tag{11}$$

Note that the tunnelling rates Γ_L and Γ_R do not enter the equations in a symmetric way. This is because the escaping process (Γ_R) kills the coherence of the system (the last term in equations (10) and (11)) but the incoming process (Γ_L) just creates an electron in the left dot (the last term in equation (8)). Figure 6(*b*) shows the time evolution of the density matrix element, ρ_LL, calculated for the initial state, $\rho(t = 0) = |L\rangle\langle L|$. As Γ_R increases, the coherent oscillation degrades more quickly and finally disappears. The total number of electrons escaping to the right electrode is obtained by

$$n_\mathrm{t}(T) = \int_0^T \rho_\mathrm{RR}(t)\Gamma_\mathrm{R}\,\mathrm{d}t, \tag{12}$$

and the time-averaged current $I_\mathrm{t} = en_\mathrm{t}(T)/T$ corresponds to the measurable current through the device. This current I_t depends on the electron occupation in the right dot, $\rho_\mathrm{RR}(t = 0)$, providing projective measurement of the charge qubit.

2.3. Coherent control of charge qubit in a DQD

A DQD device may contain a few tens of electrons basically forming many-body states. In a simplified picture, even if the dots contain more than one electron, one *excess* electron added to the DQD occupies either the right or the left dot. Each charge state involves a ground state

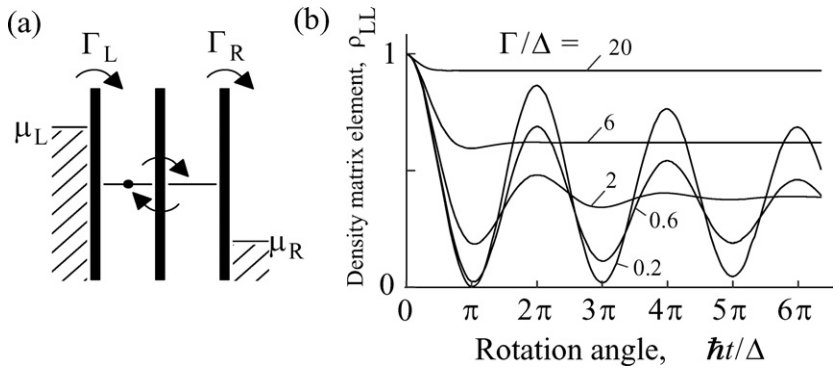

Figure 6. (*a*) Schematic energy diagram in the transport regime of a DQD. (*b*) Time evolution of density matrix element, ρ_{LL}, under initial condition, $\rho_{LL} = |L\rangle\langle L|$. $\Gamma = \Gamma_L = \Gamma_R$.

and excited states corresponding to the orbital degree of freedom in each dot. Therefore, the two-level system (qubit) given by equation (2) is a good approximation when only one well-defined state from each dot is considered as $|L\rangle$ or $|R\rangle$. This can be justified under a condition where excitation energies, like the thermal energy (2.5 μeV at 30 mK for the measurement described below), are much smaller than the characteristic energies of the dot, i.e. the addition energy (2–3 meV for typical DQD), the single-particle excitation energy (50–200 μeV), and the electrostatic coupling energy (about 100 μeV).

To observe the Larmor precession of charge qubit in a DQD, we introduce a rectangular voltage pulse to the drain electrode, as shown in figure 7(*a*). The fast voltage pulse switches the source–drain bias voltage, V_{sd}, between V_H in the transport regime and V_L ($\sim$0) in the Coulomb blockade regime, as shown in figure 7(*b*). At the same time, it also switches the energy bias ε abruptly between ε_0 (for V_H) and ε_1 (for V_L), since the DQD is also capacitively coupled to the electrodes. This simple rectangular pulse is sufficient for performing initialization, coherent manipulation and read-out processes sequentially.

When the DQD is in the Coulomb blockade region ($V_{sd} = V_L \sim 0$), tunnelling processes between the DQD and the electrodes are energetically forbidden, as shown in the energy diagram of figure 7 (*d*). Therefore, to the lowest approximation, the coupling to the electrode can be ignored and the closed two-level system discussed in section 2.2 can be applied. Other decoherence will be discussed in section 2.4. In contrast, when a large source–drain voltage ($V_{sd} = V_H$) is applied, single-electron tunnelling current flows through a DQD and the allowed tunnelling processes induce significant decoherence to the charge qubit. The corresponding energy diagrams at a large positive voltage are shown in figures 7(*c*) and (*e*). In this case, an electron in the right dot may escape to the right electrode, while another electron may enter the left dot from the left lead. Under the condition, $\Gamma_L, \Gamma_R \gg T_c$, the stationary solution of the master equation (equations (8)–(11)) becomes a density matrix with element $\rho_{LL} \sim 1$, which describes an electron confined in the left dot [21].

Therefore, the decoherence of the qubit can be switched on (in the transport regime) and off (in the Coulomb blockade regime) by changing the voltage. Our approach is to first prepare a confined state $|L\rangle$ in the transport regime and switch the system into the Coulomb blockade regime by applying a rectangular voltage pulse of an adjustable length, t_p. Since $|L\rangle$ is no longer an eigenstate in the Coulomb blockade regime, coherent time evolution is expected. After the pulse, the DQD is again set in the transport regime, so that the electron, if it occupies the right dot, contributes to the current. With this scheme, we expect one electron tunnelling per

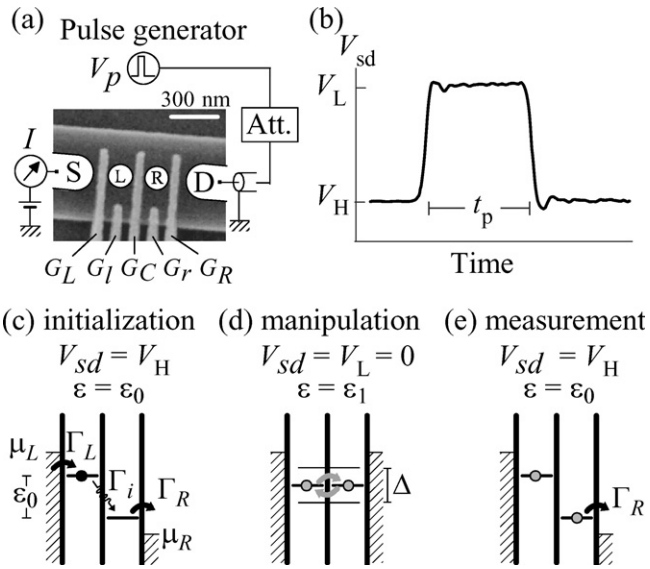

Figure 7. (*a*) Measurement setup and a SEM image of a DQD sample. A pulse generator is connected to the drain electrode through a coaxial cable. (*b*) Typical pulse waveform used for coherent control of the qubit. (*c*)–(*e*) Schematic energy diagrams of the DQD during initialization (*c*), manipulation (*d*) and measurement (*e*).

pulse at most. By repeating the pulse with repetition frequency, $f_{\mathrm{rep}} = 100\,\mathrm{MHz}$, a reasonable pumping current, $I_{\mathrm{p}} = e\rho_{\mathrm{RR}}(t_{\mathrm{p}})f_{\mathrm{rep}}$, is obtained, where $\rho_{\mathrm{RR}}(t_{\mathrm{p}})$ is the probability of finding an electron in the right dot after the pulse length t_{p}, and this provides a projective measurement.

In practice, inelastic transition contributes to an additional current during the initialization and measurement period (when $V_{\mathrm{sd}} = V_{\mathrm{H}}$). In order to reduce the effect of inelastic current on the measurement, we employ a lock-in technique to measure modulation current, I_{mod}, by turning on and off the pulse sequence with low frequency (100 Hz). Then,

$$I_{\mathrm{mod}} = [e\rho_{\mathrm{RR}}(t_{\mathrm{p}}) - t_{\mathrm{p}}I_{\mathrm{inel}}]f_{\mathrm{rep}} \tag{13}$$

should be measured.

Full one-qubit operation can be obtained by combining a rotation gate for controlling θ and a phase-shift gate for ϕ in equation (4). The rotation gate, which changes the occupation of the electron, can be performed with finite Δ at $\varepsilon = 0$, where the state rotates about the x-axis as shown in the inset of figure 8(*a*). The observed pulse-modulated current I_{mod} (circles) in this situation clearly shows an oscillating behaviour as a function of t_{p} and is fitted well with an exponentially damping sinusoidal function (solid line in figure 8(*a*)). From the fitting, the oscillation frequency in this particular case is estimated to be $f_{\mathrm{osc}} = 2.3\,\mathrm{GHz}$. The dashed line shows the inelastic current contribution, the second term of equation (13). The oscillation frequency can also be controlled by tuning the centre gate voltage, V_{C}, which mainly changes the central barrier height and thus the coupling energy, Δ. As shown in figure 8(*b*), the oscillation frequency is an exponential function of V_{C}, as expected from the tunnelling probability for realistic potential.

The amplitude of the oscillation is approximately half of the ideal case of $ef_{\mathrm{rep}} = 16\,\mathrm{pA}$. This degradation might have arisen from the population of other excited states during initialization. This could happen when the applied source–drain voltage (V_{H}) is higher than the single particle excitation energy. Or non-ideal pulse waveform (finite rising time or jittering)

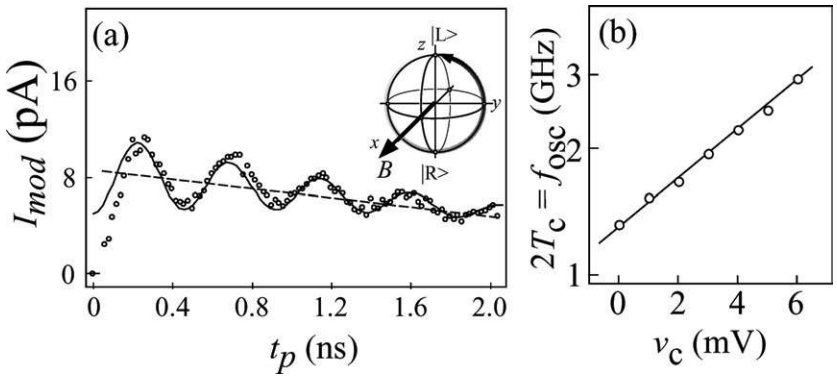

Figure 8. (*a*) Pulse-modulated current, I_{mod}, as a function of pulse length, t_{p}. The dots are the experimental data. The solid line is a fitting function. The dotted line is the offset of the oscillation. The inset shows the schematic trajectory on the Bloch sphere. (*b*) Dependence of the coherent oscillation frequency on the central gate voltage. The line is an exponential function of the center gate voltage, V_{C}. Note that the vertical axis is on a logarithmic scale.

could have influenced the rotation gate operation. The decay of the oscillation is attributed to decoherence, which is discussed in the next subsection.

An ideal phase-shift gate can be realized with finite ε at $\Delta = 0$, but this cannot be achieved in the experiment since Δ is always positive. Therefore, we approximate the phase-shift gate by applying $\varepsilon \gg \Delta$, where the state precesses more or less about the z-axis. To demonstrate the phase-shift operation that does not change electron population, we apply the pulse waveform shown in figure 9(*a*). A sharp tipping pulse of length t_{t}, which works as phase shift gate, is added at the center of the square pulse for the π-rotation gate (NOT gate) [20]. As a result, the first $\pi/2$ pulse rotates the qubit state from $|L\rangle$ to a superposition state, $(1/\sqrt{2})(|L\rangle - \mathrm{i}|R\rangle)$ on the equator, as shown by arrow (i) in the inset of figure 9(*b*). The sharp tipping pulse induces a phase difference ϕ, resulting in a state $(1/\sqrt{2})(|L\rangle - \mathrm{i}\exp(\mathrm{i}\phi)|R\rangle)$, as shown by arrow (ii). Then, the final state after the second $\pi/2$ pulse becomes $\sin(\phi/2)|L\rangle + \cos(\phi/2)|R\rangle$ (arrow (iii)), whose probability for $|R\rangle$, $\cos^2(\phi/2)$, should be measured as the corresponding pulse induced current, I_{mod}. The phase shift ϕ is approximately given by the area of the pulse (hatched region) as $\phi \simeq \varepsilon_{\mathrm{t}} t_{\mathrm{t}}/\hbar$. Actually, we change the height of the tipping pulse, ε_{t}, while keeping the pulse width constant at $t_{\mathrm{t}} \sim 55$ ps. Figure 9(*b*) shows I_{mod} obtained in this way, and the obtained oscillation indicates the phase-shift operation on the qubit. Since the oscillation is obtained with a fixed pulse width, the amplitude decay at higher V_{t} implies an increased decoherence rate at large V_{sd}.

2.4. Decoherence mechanisms

One of the most important quality factors for qubits is the phase coherence time, T_2, which is the time a qubit remains in a superposition state. In spite of the successful manipulation of a single-charge qubit, the qubit is actually influenced by uncontrolled decoherence, which is present even in the Coulomb blockade regime. Some possible decoherence mechanisms are summarized here.

First, background charge noise ($1/f$ noise) in the sample and electrical noise in the gate voltages cause fluctuation of the qubit parameters ε and T_{c}, which gives rise to decoherence of the system [18,69,70]. The amplitude of low-frequency fluctuation in ε is estimated to be about 1.6 μeV, which is obtained from low-frequency noise in the single-electron current, or 3 μeV,

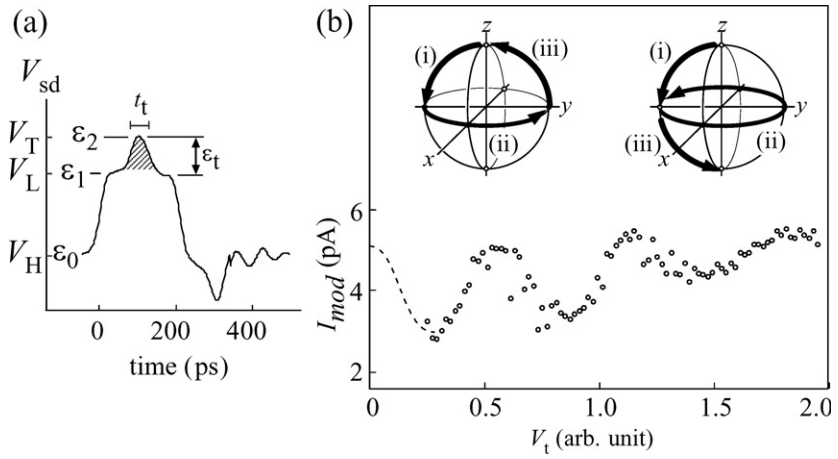

Figure 9. (*a*) Pulse shape used for phase-shift gate operation. A shape tipping pulse (hatched region) is added at the middle of the π pulse. (*b*) Dependence of the pulse-induced current $I_{\rm mod}$ on the tipping-pulse height $V_{\rm t}$, demonstrating the phase-shift operation. The insets show schematic trajectories in the Bloch sphere. The left and right inset corresponds to phase shifts $\phi = \pi$ and 2π, respectively.

which is estimated from the minimum line width of an elastic current peak at the weak coupling limit [29]. Low-frequency fluctuation in Δ is relatively small and estimated to be about 0.1 μeV at $\hbar T_{\rm c} = 10\,\mu$eV, assuming local potential fluctuation in the device [71]. Actually, the ε fluctuation explains the decoherence rate observed at the off-resonant condition ($|\varepsilon| \gtrsim \hbar T_{\rm c}$). The $1/f$ charge fluctuations are usually considered to be an ensemble of bistable fluctuators, like electron traps, each of which produces a Lorentzian frequency spectrum [26]. The microscopic origin of the charge fluctuators is not well understood, and their magnitude differs from sample to sample, even when samples are fabricated in the same batch. Understanding the fluctuators is a practical and important issue in developing quantum information devices. A recent noise measurement has indicated that the fluctuation in ε can be reduced by decreasing the temperature as suggested by a simple phenomenological model where the activation energy of the traps is uniformly distributed in the energy range of interest [71]. Cooling samples very slowly with positive gate voltage is sometimes effective in reducing charge fluctuation at low temperature [72].

In contrast, the decoherence at the resonant condition ($\varepsilon = 0$) is dominated by other mechanisms. Although the first-order tunnelling processes are forbidden in the Coulomb blockade regime, higher-order tunnelling, namely co-tunnelling, processes can take place and decohere the system [73]. Actually, the co-tunnelling rate estimated from the tunnelling rates is close to the observed decoherence rate and may thus be a dominant mechanism in the present experiment [18]. However, since we can reduce the co-tunnelling effect by making the tunnelling barrier less transparent, we should be able to eventually eliminate it in future measurements.

The electron–phonon interaction is an intrinsic decoherence mechanism in semiconductor QDs. Spontaneous emission of an acoustic phonon persists even at zero temperature and causes an inelastic transition between the two states [29]. Actually, the negative background slope shown by the dashed line in figure 8(*a*) corresponds to the inelastic tunnelling transition at the off-resonant condition ($\varepsilon = \varepsilon_0$) during the initialization/measurement sequence. The energy relaxation time in this case is about 10 ns, but becomes shorter at the resonant condition ($\varepsilon = 0$). The phonon emission rate at the resonant condition cannot be directly estimated from

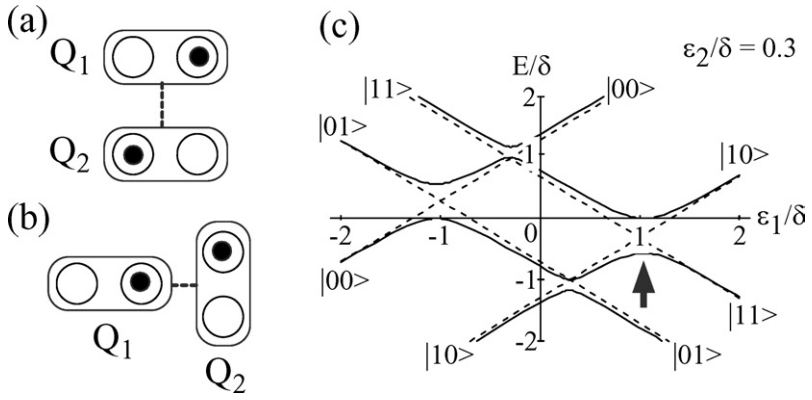

Figure 10. (*a*) Schematic diagram of two charge qubits (Q_1 and Q_2) in a parallel configuration. A round square represents a charge qubit with two QDs (○), one of which accommodates an electron (●). (*b*) Two charge qubits in a perpendicular configuration. (*c*) Energy diagram of a parrarel two-qubit system. Dashed lines are obtained under zero tunnelling coupling ($\Delta_1 = \Delta_2 = 0$); solid lines are for finite coupling ($\Delta_1 = \Delta_2 = 0.3\delta$).

this data, but it may be comparable to the observed decoherence rate. It should be noted that a measurement from a single vertical QD has also shown a phonon emission rate of the order of 10 ns (described in section 3.2) [41]. Strong electron–phonon coupling is related to the fact that the corresponding phonon wavelength is comparable to the size of the QD [27, 29]. In this sense, electron–phonon coupling may be reduced by using much smaller or much larger QD structures. In addition, polar semiconductors, such as GaAs, exhibit a piezoelectric type of electron–phonon coupling, which is significant for low-energy excitations (<0.1 meV for GaAs) [74]. Non-polar semiconductors, such as Si or carbon-based molecules, may be preferable for reducing the phonon contribution to the decoherence.

Other mechanisms, such as the electromagnetic environment, have to be considered to fully understand the decoherence. It should be noted that the quality of the coherent oscillation has actually been improved by reducing high-frequency noise from the gate voltages and a coaxial cable. We expect that further studies will exploit ways to reduce some decoherence effects.

2.5. Towards two-qubit manipulation

The CNOT gate is a nontrivial two-qubit gate, which flips the target qubit only when the control qubit is in logical one state. The experimental implementation of the CNOT gate for a charge qubit was motivated by Barenco *et al* [22], and some realistic device geometries have been proposed [23, 75]. For two qubits arranged parallel to each other as in figure 10(*a*), the state of the control qubit Q_1 modifies the energy bias, ε_2, of the target qubit, Q_2, via the Coulomb interaction. The coupling term, $\delta\sigma_{1z}\sigma_{2z}$, appears in the system Hamiltonian, where δ is the coupling energy and σ_{nz} is the z-component of the Pauli matrix of the nth qubit. When the two qubits are arranged perpendicularly as in figure 10(*b*), the coupling term is given by $\delta'\sigma_{1z}\sigma_{2x}$, where the state of the control qubit, Q_1, modifies the tunnelling coupling of the target qubit, Q_2.

Realistic devices may contain both terms in the Hamiltonian, but it is instructive to consider only one term in order to understand how the CNOT gate can be implemented. Figure 10(*c*) shows an energy diagram of two parallel charge qubits with Hamiltonian

$$H = \frac{1}{2}\left(\varepsilon_1\sigma_{1z} + \Delta_2\sigma_{1x} + \varepsilon_2\sigma_{2z} + \Delta_2\sigma_{2x} + \delta\sigma_{1z}\sigma_{2z}\right). \tag{14}$$

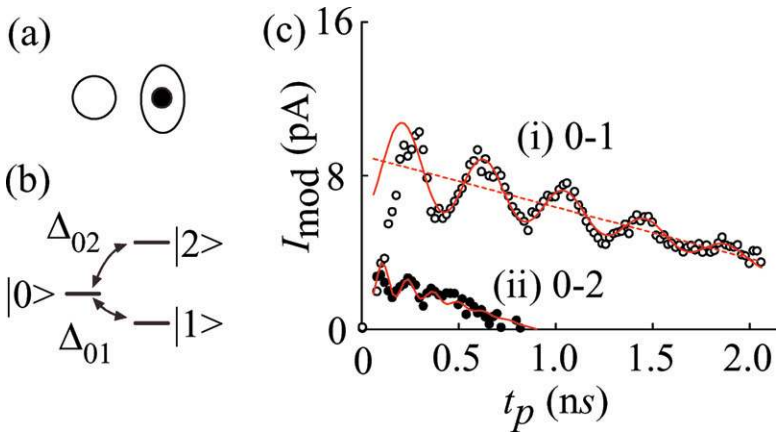

Figure 11. (*a*) Schematic diagram of an asymmetric DQD. (*b*) Energy diagram of the three-level system formed in asymmetric DQD. (*c*) Coherent oscillations taken at different resonant conditions (i) between the ground state of the left dot to the first excited state of the right dot and (ii) between the ground state of the left dot to the second excited state of the right dot.

Here, tunnelling coupling is assumed to be identical for the two qubits ($\Delta_1 = \Delta_2 = \Delta$), and eigenenergies are plotted for the energies normalized to the coupling energy δ. Anticrossing behaviour between different logical qubit states can be controlled by tuning the energy bias, ε_1 and ε_2, of the two qubits. When the system is adjusted at the anticrossing point of $|10\rangle$ and $|11\rangle$ states (shown by the arrow), coherent oscillation between these states is expected. The half period of the oscillation swaps states $|10\rangle$ and $|11\rangle$, providing a controlled-rotation (CROT) gate. A CNOT gate can also be realized by combining additional one-qubit operations.

However, the coupling term is always present in the geometries shown in figures 10(*a*) and (*b*). Therefore, the one-qubit operation in the two-qubit system is constrained to combine a couple of pulses for decoupling two qubits. For instance, combination of coherent oscillations between $|10\rangle$ and $|11\rangle$ states and between $|00\rangle$ and $|01\rangle$ states can be used for a one-qubit rotation gate for the second qubit. Although constant coupling is not an intrinsic problem for the quantum computing scheme, electrical tuning of the coupling may be useful for performing one- and two-qubit operations in more complicated systems.

Tuneable coupling can be achieved by introducing an excited state into one of the two QDs. Consider an asymmetric DQD consisting of a small QD with its ground state $|0\rangle$ and a larger QD with its ground state $|1\rangle$ and the first excited state $|2\rangle$, as shown in figures 11(*a*) and (*b*). There are tunnelling couplings, Δ_{01}, between $|0\rangle$ and $|1\rangle$ and Δ_{02} between $|0\rangle$ and $|2\rangle$, providing a three-level system. Such a three-level system is available in a realistic DQD device [76]. Actually, coherent oscillations have been observed for two resonant tunnelling conditions at slightly different gate voltages as shown in figure 11(*c*) [18]. The two oscillations correspond to coupling Δ_{01} and Δ_{02} in the three-level system.

Then, we can use the coherent oscillation between $|0\rangle$ and $|1\rangle$ for a one-qubit manipulation at the resonant condition where excitation to $|2\rangle$ is negligible. A superposition of $|0\rangle$ and $|1\rangle$ is useful for constructing a CROT gate with a neighbouring qubit, as described above. π-rotation at the other resonant condition exchanges probability amplitudes of $|0\rangle$ and $|2\rangle$, resulting in a local superposition of $|0\rangle$ and $|2\rangle$ states. Since this local superposition occupies the right dot only, its Coulomb interaction to the neighbouring qubit is almost independent of the qubit state. Therefore, a three-level system in a DQD is of interest for tuneable coupling in an integrated system.

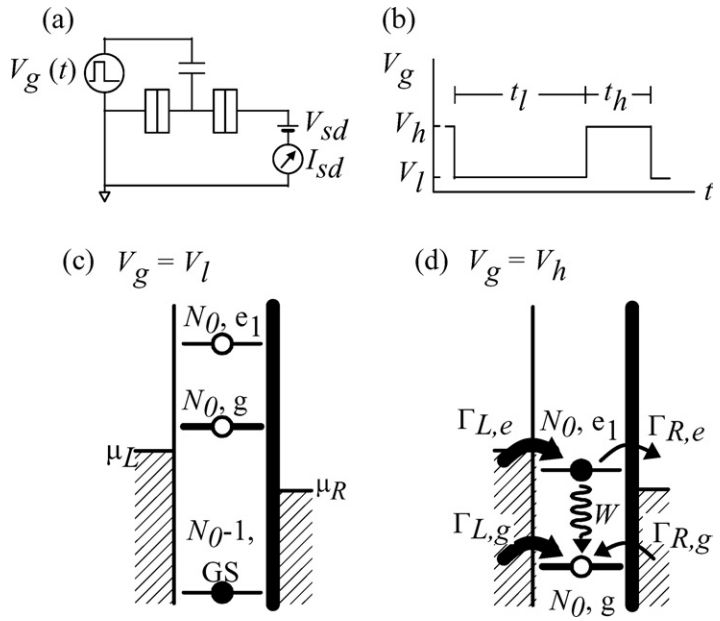

Figure 12. (*a*) Schematic diagram of the pulse measurement setup. (*b*) The pulse waveform for the single-step pulse measurement. (*c*),(*d*) Schematic energy diagrams for the low-voltage and the high-voltage states, respectively.

3. Relaxation dynamics in a QD

In this section, we discuss energy relaxation dynamics in quantum dots, which is related to the T_1 of qubit dynamics. After electrical pump–probe methods for measuring the relaxation time are described, some important relaxation mechanisms of orbital- and spin-degree of freedom in QDs are discussed based on some experiments.

3.1. Electrical pump–probe measurement

We start with single-step pulse measurement as schematically shown in figures 12(*a*) and (*b*) where a rectangular-shaped voltage pulse, $V_g(t)$, is applied to the gate electrode [77]. Consider the relaxation process from a first excited state (ES) to the ground state (GS) of N_0-electron QD. First, the QD is set in the $N = N_0 - 1$ CB state when the gate voltage is in the low-voltage state, $V_g = V_l$, as shown in figure 12(*c*). We also tune the two tunnel barriers such that the tunnel rate through the left entrance barrier, Γ_L, is much larger than that through the right exit barrier, Γ_R. After a sufficiently long time period, $t_l \gg \Gamma_L^{-1}$, the QD is prepared in $N = N_0 - 1$ GS. In this situation, both N_0-electron GS and ES of interest are above the chemical potential of the two electrodes, μ_L and μ_R. Next, V_g is switched to V_h (high-voltage state) within a short time, which should be comparable to or shorter than Γ_L^{-1}. We adjust V_h such that only the ES is located in the transport window between μ_L and μ_R, as shown in figure 12(*d*). Here, the QD is in the N_0-electron CB region. The applied voltage, $eV_{sd} = \mu_R - \mu_L$, should be larger than $\hbar\Gamma_L$ to prevent the back-flow of the electron to the left electrode. Then, an electron can enter the GS (ES) with a probability proportional to the rate, $\Gamma_{L,g} + \Gamma_{R,g}$ ($\Gamma_{L,e}$). If an electron enters the ES, it can either tunnel out to the right electrode to give a net current, or relax to the GS. When the barriers are highly asymmetric ($\Gamma_L \gg \Gamma_R$), the electron can stay in the ES for a

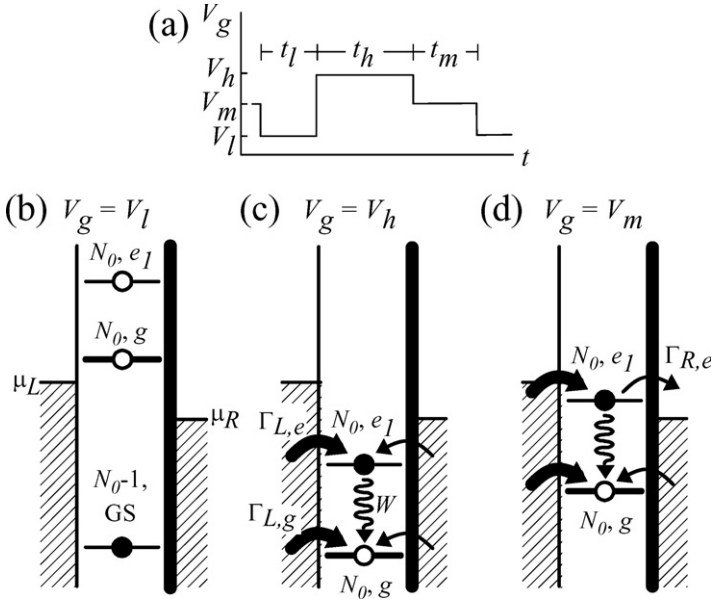

Figure 13. (*a*) Pulse waveform for the double-step pulse measurement. (*b*), (*c*), (*d*) Schematic energy diagrams for the low-, high- and medium-voltage states, respectively.

relatively long time, $\sim\Gamma_{\mathrm{R}}^{-1}$, during which relaxation may take place. If the electron in the ES tunnels out to the right electrode, another electron enters the ES or GS. However, this cycle is terminated once the GS is occupied, either by relaxation from the ES or by direct tunnelling from the electrodes.

The average number of tunnelling electrons per pulse, n_{t}, is given as

$$n_{\mathrm{t}} = n_{\max}[1 - \exp(-Dt_{\mathrm{h}})] \tag{15}$$

by solving rate equations [78, 79]. Here, $n_{\max}$ is the maximum number of tunnelling electrons obtained with sufficiently long t_{h} and t_{l}, and D is the decay rate of the transient current. This D gives the relaxation rate W of interest provided that $\Gamma_{\mathrm{L}} \geqslant W \geqslant \Gamma_{\mathrm{R}}$. One can determine W from this relation. The pulse length dependence of n_{t} shown in figure 16 is obtained in this way.

If the bias is reversed (thicker emitter barrier), on the other hand, the decay rate is insensitive to W, as given by $D \sim \Gamma_{\mathrm{tot,g}} = \Gamma_{\mathrm{L,g}} + \Gamma_{\mathrm{R,g}} \sim \Gamma_{\mathrm{L,g}}$. This situation can be used to determine the total tunnelling rate, $\Gamma_{\mathrm{tot,g}}$. Another way to obtain $\Gamma_{\mathrm{tot,g}}$ is to vary t_{l} with t_{h} fixed at a long-enough value, $t_{\mathrm{h}} \gg \Gamma_{\mathrm{R}}^{-1}$, corresponding to the escaping process from the GS to either electrode as shown in figure 12(*c*). In this case, the average number of tunnelling electrons per pulse is given by

$$n_{\mathrm{t}} = n_{\max}[1 - \exp(-\Gamma_{\mathrm{tot,g}} t_{\mathrm{l}})], \tag{16}$$

from which $\Gamma_{\mathrm{tot,g}}$ can be determined by fitting the data to this equation. Since an asymmetric barrier is not required, this method can be used for various situations.

The above single-step pulse method is unable to determine the relaxation rate if $W < \Gamma_{\mathrm{R,e}}$ (long relaxation time), as in the case of the relaxation involving a spin flip. Such a case requires an improved method involving the application of a double-step voltage pulse, where V_{g} is switched between three voltages, V_{l}, V_{h} and V_{m}, as shown in figure 13(*a*).

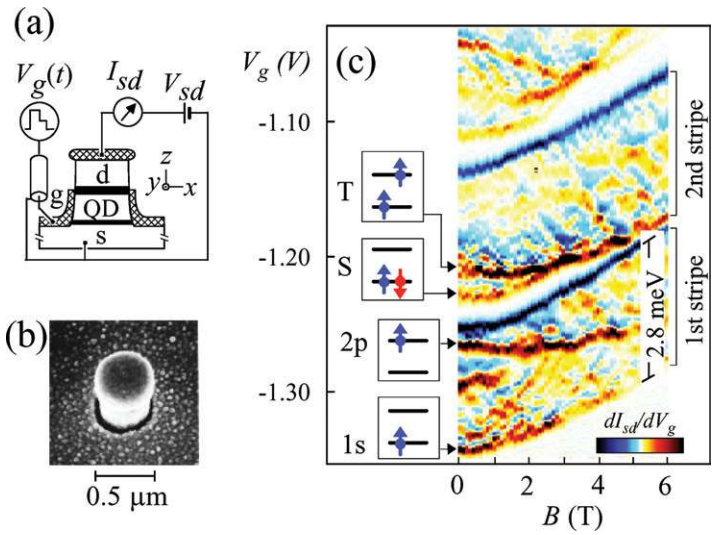

Figure 14. (*a*) Schematic diagram of a vertical QD together with the pulse measurement set-up. (*b*) Scanning electron micrograph of the vertical dot device. (*c*) $\mathrm{d}I_{\mathrm{sd}}/\mathrm{d}V_{\mathrm{g}}$ for $N = 1$ (first stripe) and 2 (second stripe) measured with $V_{\mathrm{sd}} = 2.8\,\mathrm{mV}$ at temperature $T \sim 100\,\mathrm{mK}$.

First, when $V_{\mathrm{g}} = V_{\mathrm{l}}$, the $N = N_0$ GS and ES are above the chemical potential as shown in figure 13(*b*). The GS and ES are emptied by maintaining this condition for a sufficiently long time, t_{l} (initialization). Next, by instantly changing V_{g} to V_{h}, both states are pulled down below the electrochemical potential of the electrode as shown in figure 13(*c*). Now, an electron enters either ES or GS (arrows). Once an electron enters the dot, it cannot leave the dot because large energy is required in order to excite the electron to the electrode, nor can another electron enter the dot (Coulomb blockade). This electron, if it populates the ES with a probability P, is allowed to relax to the GS while the gate voltage is kept at V_{h} during the wait time t_{h}. Finally, the pulse height is adjusted so that only the ES is within the transport window between μ_{L} and μ_{R} (read-out). Then, the electron can contribute to the current only if it remains in the ES after t_{h}. This read-out pulse width, t_{m}, is made sufficiently longer than Γ_{R}^{-1}. Actually, several electrons $[1/(1-P)]$ flow during this time for the unrelaxed case. Therefore, the average number of tunnelling electrons per pulse cycle, n_{t}, follows an exponential decay,

$$n_{\mathrm{t}} = \frac{P}{1-P}\exp(-Wt_{\mathrm{h}}), \tag{17}$$

from which the relaxation rate W can be determined [41]. Thus, the double-step pulse scheme clearly separates pumping and probing sequences and is applicable to a wide range of $W \ll \Gamma_{\mathrm{L}}$. The lower limit is practically determined by current sensitivity. Spin relaxation measurement data shown in figure 17 are obtained with this technique.

3.2. Momentum relaxation

The QD devices discussed in section 2 are called 'lateral' dot device because current flows laterally. There is another type of QD called a 'vertical' dot, which is shown in figures 14(*a*) and (*b*). It is in the form of a submicron-sized circular mesa fabricated from an AlGaAs/InGaAs/AlGaAs double barrier structure. Current flows vertically through the mesa, and the electron number, N, in the dot formed in the InGaAs layer is changed using a

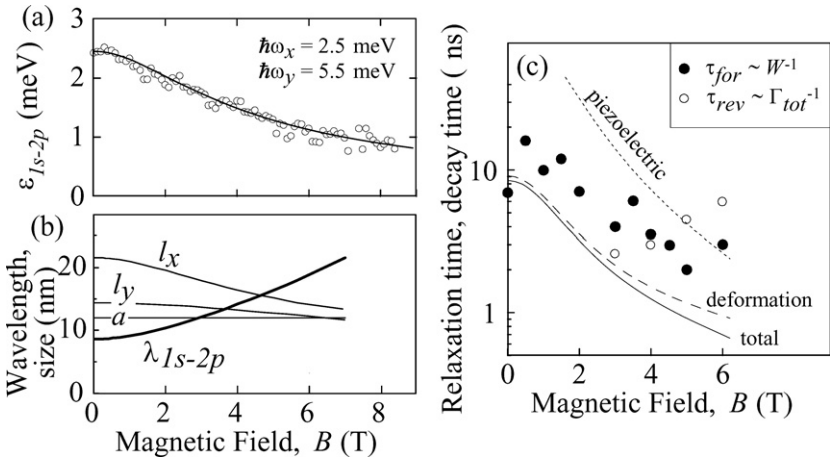

Figure 15. (*a*) Energy difference between 1s and 2p states, ε_{1s-2p} in the $N = 1$ QD. (*b*) Size of the QD (a, l_x and l_y) and the phonon wavelength, λ_{1s-2p}, corresponding to the energy spacing. (*c*) Decay time of the transient current for forward bias (●) and reverse bias (○), and energy relaxation times calculated from the piezoelectric potential (· · · · · ·), or the deformation potential (- - - -), and both potentials (——).

gate electrode wrapped around the mesa. Electronic states (spin S and total angular momentum M) and N can be unambiguously determined in a vertical QD owing to the well-defined lateral confinement potential (approximately harmonic potential) and to a built-in tunnel rate via the AlGaAs barriers [16]. The first few electrons occupy 1s ($M = 0$) and 2p ($M = \pm 1$) orbitals, which have two-fold and four-fold degeneracy including spin, respectively. This results in a 'shell structure' in the Coulomb blockade oscillation characteristics, where large energy gaps appear at $N = 2$ ($N = 6$) when the 1s (2p) orbital is fully occupied by electrons, just as in real atoms.

Although the nominal dot shape is circular, a specific QD used for the relaxation measurement has non-circular lateral confinement potential in the x–y plane with confinement strength, $\hbar\omega_x = 2.5$ meV and $\hbar\omega_y = 5.5$ meV. Therefore, degeneracy of the two 2p states with ($M = \pm 1$) is already lifted at $B = 0$. Despite this non-circularity, we still use the terms '1s' and '2p' to label states for convenience.

Figure 14(*c*) shows excitation spectra, $\mathrm{d}I_{\mathrm{sd}}/\mathrm{d}V_{\mathrm{g}}$, as a function of magnetic field with a large source–drain bias, $V_{\mathrm{sd}} = 2.8$ meV [17]. Positive peaks in the 1st (2nd) stripe correspond to electron injection to ground and excited states of the $N = 1$ ($N = 2$) QD. GS and ES are designated by arrows together with schematic electron configurations in the inset, in which the lower (upper) horizontal bar represents the 1s (2p) orbital. Here, we are not able to resolve small Zeeman splitting (∼0.1 meV at 5 T). The energy difference between the 1s and 2p states, ε_{1s-2p}, estimated from the 1st stripe of the excitation spectra in figure 14(*c*) is plotted in figure 15(*a*). The solid line shows a fitted theoretical calculation based on the asymmetric parabolic confinement potential (confinement energies $\hbar\omega_x$ and $\hbar\omega_y$) in the x–y plane [80]. The corresponding characteristic size of the QD in the x/y direction is given by

$$l_{x/y} = \sqrt{\hbar/m^*}(\omega_{x/y}^2 + \omega_{\mathrm{c}}^2/4)^{-1/4}, \tag{18}$$

where m^* and $\hbar\omega_{\mathrm{c}}$ are the effective mass and cyclotron energy, respectively. The magnetic field dependence of these characteristic lengths is plotted in figure 15(*b*).

We apply the single-pulse measurement scheme to extract momentum relaxation time in the $N = 1$ QD, which can be regarded as an artificial hydrogen atom. In this case, an electron

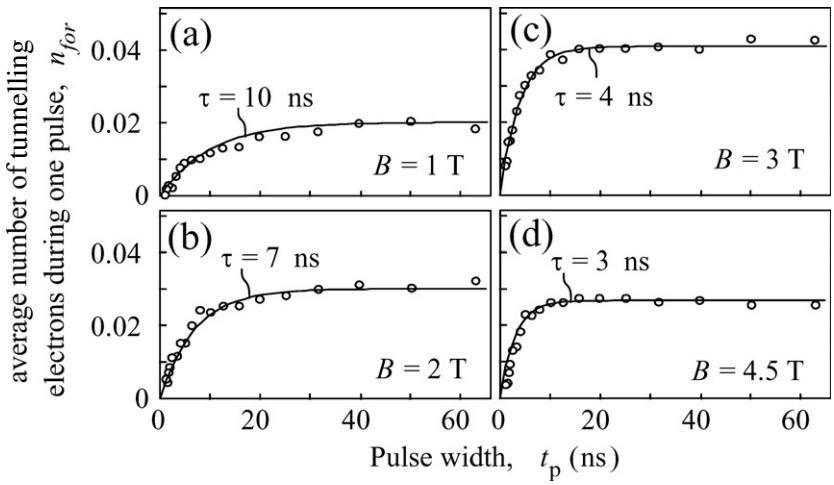

Figure 16. Average number of tunnelling electrons per pulse, n_{for}, in the forward bias for different magnetic fields.

relaxes from the 2p state to the 1s state, preserving the spin. The dot is coupled to the top and bottom electrode with $\Gamma_{\mathrm{t}}^{-1} \sim 100$ ns and $\Gamma_{\mathrm{b}}^{-1} \sim 3$ ns, reflecting the built-in asymmetric AlGaAs barriers. Figure 16 shows the average number of tunnelling electrons per pulse, n_{for} in the forward bias for different magnetic fields, i.e. different $\varepsilon_{1\mathrm{s}-2\mathrm{p}}$. Each data point is fitted with equation (16) (solid line), from which the decay time, τ_{for}, in the 3–10 ns range is estimated. Although there is some scatter of data points, τ_{for} decreases systematically with B as shown by the solid circles in figure 15(*c*). We also show the decay time in reverse bias, τ_{rev}, by open circles for comparison. The increase of τ_{rev} with B is consistent with the decrease of tunnelling rate, Γ_{tot}, with B.

In this situation, with an energy difference of a few millielectronvolts and at low temperature, a dominant momentum relaxation mechanism is the spontaneous emission of an acoustic phonon [29]. The corresponding phonon wavelength is given by $\lambda_{1\mathrm{s}-2\mathrm{p}} = hv_{\mathrm{phonon}}/\varepsilon_{1\mathrm{s}-2\mathrm{p}}$, where $v_{\mathrm{phonon}} = 5100\,\mathrm{ms}^{-1}$ is the phonon velocity in GaAs. $\lambda_{1\mathrm{s}-2\mathrm{p}}$ is comparable to or even smaller than the characteristic size of the QD as compared in figure 15(*b*). The observed increase of the relaxation time with the decrease of $\lambda_{1\mathrm{s}-2\mathrm{p}}$ is in line with the inefficient phonon emission rate known as phonon bottleneck effect [81, 82]. In figure 15(*c*), we also plot calculated relaxation times based on Fermi's golden rule for the piezoelectric mechanism and deformation mechanism and for the sum of the two mechanisms [41, 83, 84]. The reasonable agreement with the experimental data in spite of the lack of fitting parameters confirms that the momentum relaxation in the $N = 1$ QD occurs via emission of a phonon.

3.3. Spin relaxation

Next, we consider the spin relaxation process in an $N = 2$ QD, which mimics a helium atom. At low magnetic field, the many-body GS is a spin singlet (S) with total spin, $S = 0$, while the first ES is a triplet state (T) with $S = 1$, as schematically illustrated in the inset of figure 14(*c*). Energy relaxation from the triplet ES to the singlet GS not only involves momentum relaxation as in the $N = 1$ QD, but also spin relaxation. Therefore, some kind of spin–flip mechanism is necessary for relaxation. Spin is generally considered to be a good quantum number, which suggests that the spin–flip process occurs over a much longer time

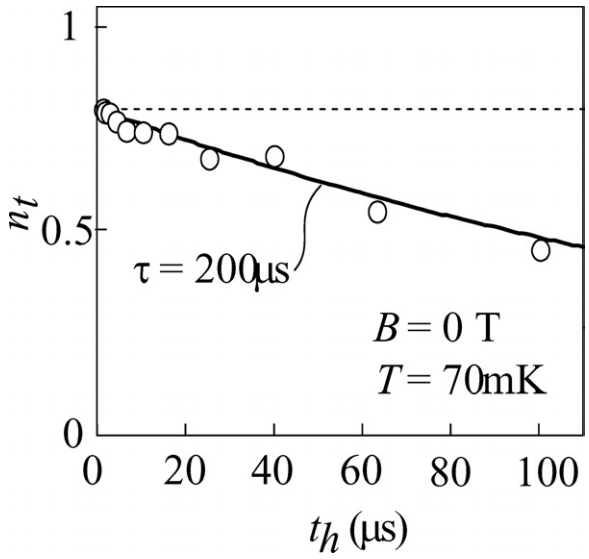

Figure 17. Relaxation time measurement for the triplet ES in the $N = 2$ QD. n_t is the average number of tunnelling electrons per pulse.

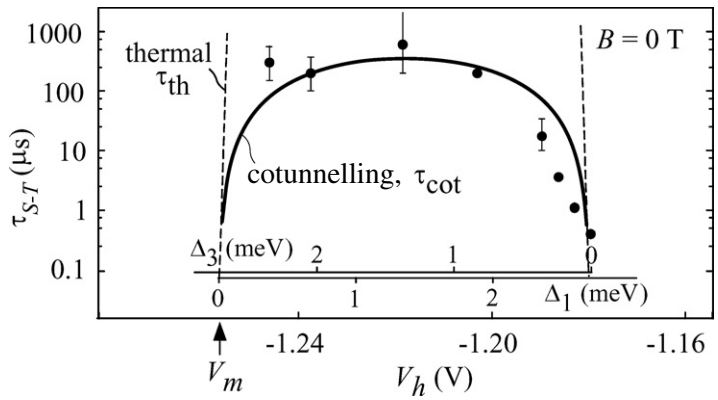

Figure 18. Spin relaxation time as a function of the high-state voltage of the double-step pulse.

scale compared with a simple phonon-emission process. Therefore, we use the double-step pulse technique explained above. Figure 17 shows the average number of tunnelling electrons per pulse, n_t, as a function of wait time, t_h, in the high-voltage state of the double-step pulse. By fitting the exponential curve (equation (17)) to the data, the spin relaxation time $\tau = 200\,\mu$s is estimated. This is four to five orders of magnitude longer than the momentum relaxation time observed for the $N = 1$ QD [85, 86]. Recently, relaxation times of longer than milli seconds have been reported in QDs between Zeeman sublevels, as well as between a spin triplet and a singlet state [34, 36, 40]. Electron spin is therefore considered to be a promising candidate for a quantum bit.

Now, the question is: what is the spin relaxation mechanism? Figure 18 shows the observed spin relaxation time as a function of the high state voltage, V_h. The energy required to excite the $N = 2$ triplet ES to $N = 1$ GS, Δ_1, increases with gate voltage, V_h, while the excitation

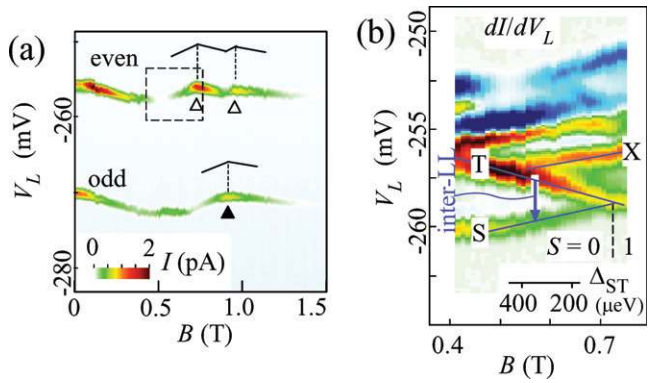

Figure 19. (*a*) Evolution of the two Coulomb oscillation peaks under magnetic field showing a spin-pair behaviour, taken at $V_{sd} = 0.15$ mV. Transition fields are denoted by triangles. (*b*) dI/dV_L at $V_{sd} = 1.2$ mV taken from the dashed rectangular region in (*a*).

energy to $N = 3$ GS, Δ_3, decreases with increasing V_h, as shown in the subordinate scales in figure 18. The observed spin relaxation time strongly depends on V_h, especially around the small Δ_1 regime. This implies a strong influence from electrodes other than the thermal excitation effect, which predicts much sharper V_h dependence, as shown by the dashed line in figure 18. Although the dot is kept at the $N = 2$ CB condition during the relaxation stage, higher-order tunnelling, or co-tunnelling, is quite effective in causing an exchange of electrons having opposite spins between the dot and the lead electrodes [87]. This results in spin relaxation from the triplet ES to the singlet GS. According to the second-order perturbation theory, the co-tunnelling rate, τ_{cot}^{-1}, is approximately given by

$$\tau_{cot}^{-1} = \Delta_{ST}(\hbar\Gamma_{tot})^2(\Delta_1^{-1} + \Delta_3^{-1})^2/h, \tag{19}$$

where $\Gamma_{tot} = \Gamma_L + \Gamma_R$ is the total tunnelling rate and Δ_{ST} the singlet–triplet energy difference [41, 88]. The solid line in figure 18(*a*) shows τ_{co} calculated from equation (19) without any fitting parameters (Γ_{tot} is obtained from a separate single-pulse measurement). The reasonable agreement with the experimental data indicates that inelastic co-tunnelling is a dominant spin relaxation mechanism in this experiment.

In a vertical QD, the tunnelling rate through the barriers is predetermined by the semiconductor crystal growth. In a lateral QD, on the other hand, we have more freedom in tuning the tunnelling rate with the gate voltages, which allows us to study spin dynamics in a wider regime where different relaxation mechanisms compete. In a lateral QD similar to the one shown in figure 1(*c*), tunnelling rates, Γ_L and Γ_R, can be changed by changing the gate voltages, V_L and V_R. Although we cannot determine the exact number of electrons, we can determine whether it is even or odd from the electron-addition spectrum. Figure 19(*a*) shows an observed dc current, I, through the dot as a function of left gate voltage, V_L, and magnetic field, B. An overall pair-wise motion of the two stripes with B reflects spin degeneracy. The electron orbitals in a few-electron QD can be classified by the Landau level (LL) index [89, 90]. The lower stripe, corresponding to odd N, involves a level crossing (denoted by a solid triangle), associated with two different LLs. As for the upper stripe with even N, the ground state is mostly spin singlet. However, direct and exchange Coulomb interactions favour a spin triplet GS via rearrangement of electrons between different LLs [45]. In our data, the triplet GS is realized between the two open triangles. These spin states can also be observed in the excitation spectrum of figure 19(*b*), where dI/dV_L, with a large $V_{sd} = 1.2$ mV, is plotted as a function of V_L and B. Some ESs as well as the GS that fall within the source–drain transport

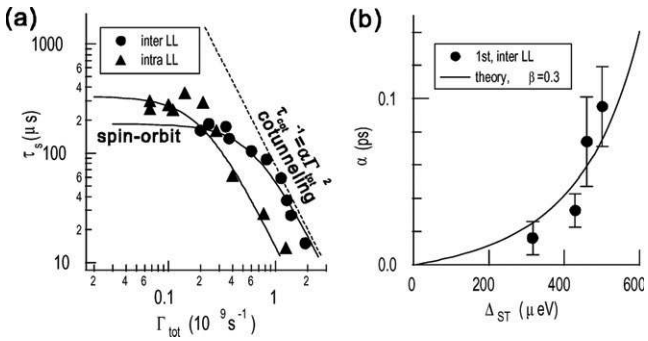

Figure 20. (*a*) Log–log plot of τ_s as a function of Γ_{tot} for both the inter-LL and intra-LL cases. The solid lines are fitted to the data. (*b*) The coefficient α for the co-tunnelling component as a function of Δ_{ST}. β is a ratio between the effective Γ_{tot} and the experimentally determined one.

window are observed. The spin relaxation denoted by the arrow involves an orbital change between different LLs (inter-LL transition).

We performed double-step pulse measurement to obtain spin relaxation time, τ_s, and total tunnelling rate, Γ_{tot}. By changing some gate voltages, we measured how τ_s changes with Γ_{tot} in the range from 1×10^8 to $3\times10^9\,s^{-1}$, as shown in figure 20(*a*). The data points at large Γ_{tot} are consistent with co-tunnelling theory, as shown by the dashed line $t_{cot}^{-1} = \alpha\Gamma_{tot}^2$ (see equation (19)). The proportional factor α depends on Δ_{ST} as shown in figure 20(*b*), which is also consistent with the theory, as shown by the solid line. Therefore, spin relaxation in the large Γ_{tot} regime can be well explained by the standard co-tunnelling theory. It is seen in figure 20(*a*) that, when Γ_{tot} is reduced, τ_s increases and eventually saturates. In this regime, the co-tunnelling process is well suppressed and intrinsic spin relaxation time, which is independent of Γ_{tot}, can be investigated. Theoretically, spin–orbit interactions are predicted to make the dominant contribution to spin relaxation in GaAs QD systems [39,91]. By assuming this prediction, the spin–orbit relaxation time, τ_{so}, can be obtained by fitting the data with $(1/\tau_{so}+1/\tau_{cot})^{-1}$ as shown by the solid line in figure 20(*a*).

3.4. Spin–orbit coupling effect

Spin–orbit interaction in III–V semiconductors originates from the absence of crystal inversion symmetry (the Dresselhaus effect), asymmetric confinement potential (the Rashba effect) and interface or surface effects [37]. For a one-electron system in a QD, these spin–orbit interaction couples a spin-up (down) state of one orbital to a spin-down (up) state of another orbital. When spin–orbit coupling is considered between the two orbitals, say a and b with matrix element $\Delta_{so} = |\langle\psi_{a,\uparrow}|H_{so}|\psi_{b,\downarrow}\rangle| = |\langle\psi_{a,\downarrow}|H_{so}|\psi_{b,\uparrow}\rangle|$, spin-up and spin-down components are mixed and finite phonon emission probability is expected between Zeeman sublevels under a magnetic field [77, 92]. This spin-mixing and electron–phonon coupling between Zeeman sublevels give the B^{-5} dependence of the relaxation time, as shown by optical excitation/detection measurement for self-organized QDs [39,40].

In the case of a two-electron state, which can be approximated by the Slater determinant of the one-electron orbitals, spin–orbit interaction gives selective mixing between different spin states. The spin singlet state ($|S\rangle$) is coupled to two of the triplet sublevels ($|T_+\rangle$ and $|T_-\rangle$) having $S_Z = \pm1$ but not to the other sublevel ($|T_0\rangle$) having $S_Z = 0$ [39,93]. Therefore, relaxation from the triplet to the singlet state should be governed by a selection rule in which

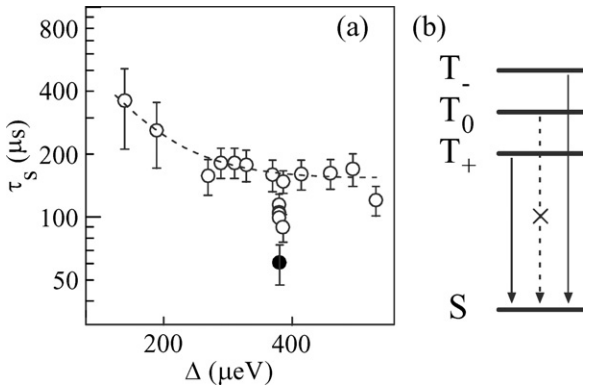

Figure 21. (*a*) Δ_{ST} dependence of the τ_s for the inter-LL relaxations. Data represented by open symbols are obtained by fitting a single exponential function, while the solid circle represents the fast component of the double exponential function. The dotted line is a guide for the eye. (*b*) Allowed and forbidden transitions from the triplet sublevels to the singlet state.

$|T_0\rangle$ state is still free from the spin–orbit relaxation mechanism as shown in figure 21(*b*). This simple argument applies when the singlet-triplet energies are so close to each other that coupling with other states is negligible.

Figure 21(*a*) shows the magnetic field dependence of τ_s measured in the small-Γ_{tot} regime where spin–orbit interaction is a dominant spin relaxation mechanism. The data are actually plotted against Δ_{ST}. τ_s is almost constant in a wide Δ_{ST} regime (except at a dip around $\Delta_{ST} \sim 380\,\mu$eV) and tends to increase when $\Delta_{ST} < 200\,\mu$eV, which might arise from the phonon emission spectra in a QD as discussed in section 3.2. The sharp dip observed at $\Delta_{ST} \sim 380\,\mu$eV is as narrow as about $20\,\mu$eV in Δ_{ST} (~ 10 mT in B). It may be related to the level crossing at $B \simeq 0.52$ T ($\Delta_{ST} \simeq 400\,\mu$eV), where the triplet state (T) crosses with another state (X) as seen in figure 19(*b*). The state X can be identified as spin singlet, since unresolved anti-crossing behaviour ($<100\,\mu$eV) is observed between X and T [80, 94, 95].

This situation suggests that strong spin–orbit coupling around the crossing point enhances the spin relaxation rate, as theoretically predicted in [92]. It should be noted that the decay of the pulse-induced current shows a non-single exponential behaviour around the dip as shown in figure 22(*b*), while single exponential decay is always observed at other conditions, e.g. at $\Delta_{ST} = 300\,\mu$eV shown in figure 22(*a*). The decay characteristic in figure 22(*b*) can be expressed well by a double exponential function (the solid line), $\frac{2}{3}\exp(-t_h/\tau_{so}) + \frac{1}{3}\exp(-t_h/\tau_{cot})$ with a 2 : 1 ratio consistent with the spin–orbit selection rule. Thus, the fast component with rate τ_{so} can be assigned to the relaxation from $|T_+\rangle$ and $|T_-\rangle$ via spin–orbit coupling and the slow component to the relaxation from $|T_0\rangle$ via remaining co-tunnelling contribution, τ_{cot}.

Although the above observations agree well with the selection rule for spin–orbit coupling, we cannot safely rule out other possibilities. Hyperfine coupling to nuclear spins might appear at the level coincidence of different spin states [42, 96]. In this case, one of the triplet states with finite Zeeman splitting can couple to the singlet state via flip–flop interaction, leading to a 1 : 2 selectivity rather than the observed 2 : 1 ratio. However, our measurement does not provide sufficient accuracy for identifying the origin of the selection rule. Identifying the mechanism requires further investigations. Nevertheless, the observed double exponential behaviour should be related to some selection rule for spin-triplet and unknown (probably singlet) states.

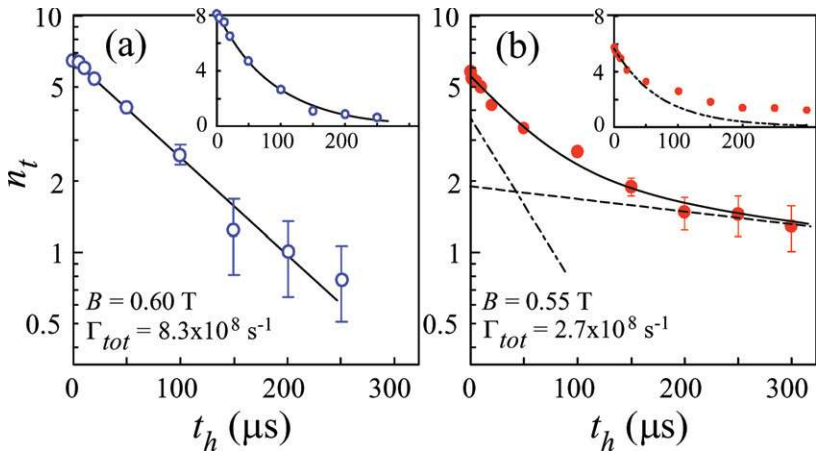

Figure 22. (*a*) Logarithmic plot of n_t versus t_h at $\Delta_{ST} = 300\,\mu$eV ($B = 0.6$ T). The solid line is an exponential function fitted to the data. (*b*) A logarithmic plot of n_t versus t_h at $\Delta_{ST} = 380\,\mu$eV ($B = 0.55$ T). The solid line is a double-exponential function fitted to the data. The dotted and dashed lines are the fast and slow components, respectively. Each inset is a linear plot of the same data.

Now, let us assume spin–orbit coupling dominates the singlet-triplet relaxation process. Then, we can think of an 'entanglement generator' using the selection rule. The singlet ground state $|S\rangle = |\uparrow\rangle_a |\downarrow\rangle_a$ holds a spin pair in an orbital a, while the triplet state contains non-entangled states, $|T_+\rangle = |\uparrow\rangle_a |\uparrow\rangle_b$ and $|T_-\rangle = |\downarrow\rangle_a |\downarrow\rangle_b$, and entangled state, $|T_0\rangle = (1/\sqrt{2})(|\uparrow\rangle_a |\downarrow\rangle_b + |\downarrow\rangle_a |\uparrow\rangle_b)$, with an electron in orbitals a and b. After a proper waiting time after electron injection into one of the four states, the system is left in the entangled triplet state $|T_0\rangle$ or the singlet ground state $|S\rangle$. Our pulse measurement is based on the extraction of an electron only from the triplet excited state, and thus this scheme can be used to generate or analyse an entangled spin pair by detecting the extracted electron with a sensitive electrometer [35, 36].

4. Statistics of single-electron tunnelling

Statistics of a transition from one state to another reflects the symmetry of the particle (boson or fermion), interaction between the particles and coupling to the environment. Single-electron tunnelling is a tunnelling transition that is influenced by Coulomb interaction inside a QD [59]. The transition is forbidden if the Coulomb energy cost for injecting an electron into the QD exceeds the excitation energy of the transition (Coulomb blockade). Tunnelling is also influenced by spin correlation (e.g. spin singlet or triplet), as shown by the Pauli spin blockade effect in transport through a DQD [97].

Such single-electron tunnelling has been discussed with conventional current measurement. However, current measurement has very low sensitivity in the sense that millions of electrons are required to obtain a meaningful current signal. In contrast, charge detection measurement allows direct detection of electron occupation in a QD and provides a sensitive measurement for single-electron transport.

4.1. Charge detection techniques

The single-electron transistor (SET), whose transport is influenced by Coulomb interaction in the QD, is known as a sensitive electrometer with expected sensitivity of about

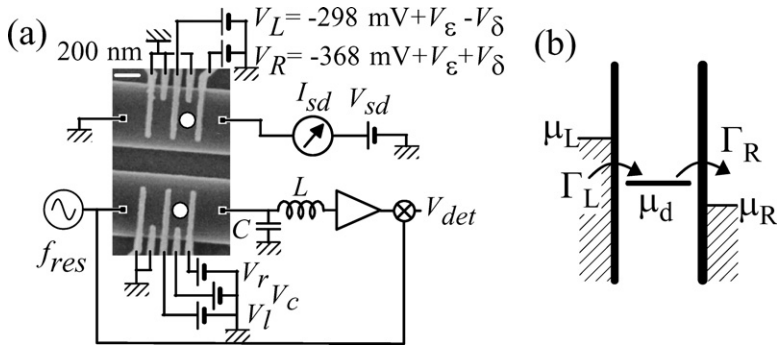

Figure 23. (*a*) Schematic diagram of the measurement setup. The sample shown in the scanning electron micrograph contains two GaAs QDs (white circles) made by a dry etching (upper, central and lower dark regions) and Schottky gates (vertical bright lines). The white bar is a scale of 200 nm. The RF carrier signal is transmitted through the lower QD and the LC resonator. The measurement was done in a dilution refrigerator ($T \sim 0.1$ K). (*b*) Energy diagram of a single-electron tunnelling process.

$10^{-6}\, e/\sqrt{\text{Hz}}$ [98, 99]. The radio-frequency (RF) technique allows us to operate such a SET with carrier signal at gigahertz frequency, and the charge detection bandwidth can exceed 100 MHz [100, 101]. Another type of electrometer can be made from a semiconductor point contact (PC) structure, which exhibits quantized conductance corresponding to the number of occupied one-dimensional channels [102–104]. Tunnelling probability for an unoccupied channel depends on the potential barrier at the contact, which is sensitive to charge distribution around the contact. Thus, these electrometers provide a charge detection scheme for QDs electrostatically coupled to the electrometer. SET electrometer has essentially better sensitivity than PC electrometer, since a large change in the transmission probability is expected. However, the practical signal-to-noise ratio remains more or less the same, when it is determined by background charge fluctuation in the device or other extrinsic noise in the measurement system. In this case, the PC electrometer has the advantage of a simpler structure, and it can be operated with fewer gate electrodes in a wide gate-voltage range.

Figure 23(*a*) shows a typical circuit diagram along with a scanning electron micrograph for charge detection measurement. Two electrically isolated channels are integrated in an AlGaAs/GaAs heterostructure [101, 105]. A QD in the lower channel works as a SET electrometer. One end of the SET is connected to an LC resonator and a low-noise high-frequency amplifier. An RF carrier signal at the resonant frequency of 650 MHz is sent from the other end of the SET, and the transmission signal is detected using a phase-sensitive detection scheme. The output voltage V_{det} is proportional to the conductance of the SET, so that the SET serves as an RFSET electrometer. This SET is coupled to the other QD formed in the upper channel. The coupling coefficient η ($\sim$0.005 in this sample) is given by the coupling capacitance between the two QDs relative to the total capacitance of the QD in the electrometer. Charging an electron to the upper QD induces a fractional charge of about $0.005e$ on the lower QD, which can be measured from a change in the electrometer output.

4.2. Charge detection of a quantum dot

Consider the two-level charge fluctuation in a QD in the single-electron tunnelling regime. Only one excess electron can occupy the QD. By assuming a single spinless energy state in the QD, as schematically shown in the energy diagram of figure 23(*b*), transport is characterized by tunnelling rates Γ_{L} and Γ_{R} across the left and right barriers, respectively [59]. The current

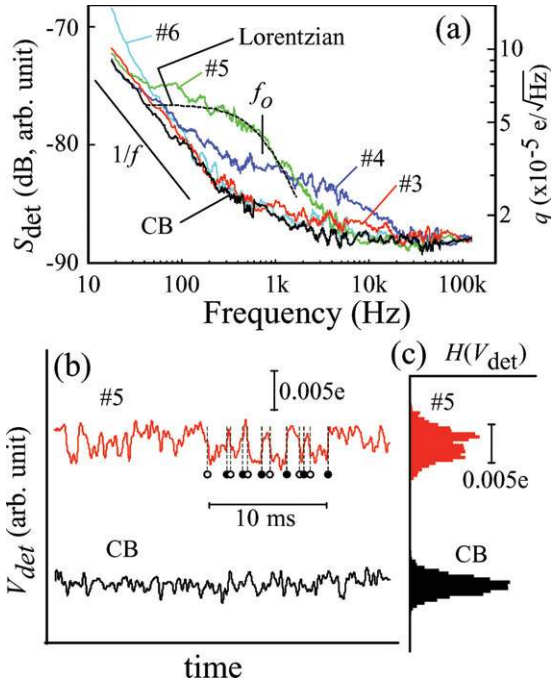

Figure 24. (*a*) Frequency spectra of the RFSET signal, $V_{\rm det}$, for CB condition and single-electron transport conditions (#3–#6). Each spectrum is obtained by averaging data for about 1 h. Sharp-peak artefacts from 50-Hz harmonics are removed for better visibility. (*b*) Time-domain measurements of $V_{\rm det}$ for CB (the lower trance) and single-electron tunnelling regime (the upper trace for #5). No averaging is performed. (*c*) Histograms, $H(V_{\rm det})$, of the two traces of (*b*) but for a longer time domain.

is defined by the net charge transfer from the left lead to the right lead. For instance, under a relatively large voltage that ensures forward tunnelling direction, the averaged current is given by $I = e\Gamma_{\rm L}\Gamma_{\rm R}/(\Gamma_{\rm L} + \Gamma_{\rm R})$. In contrast, an electrometer measures the occupation of the charge state, regardless of which lead an electron was injected from or escaped to. Therefore, it is convenient to characterize the charge fluctuation using the incoming rate ($\Gamma_{\rm in}$) and the outgoing rate ($\Gamma_{\rm out}$), respectively, for increasing and decreasing the electron number in the QD. Assuming a purely random stochastic process for tunnelling transitions, the power spectrum of the charge fluctuation is given by the Lorentzian form:

$$S_q(\omega) = \frac{4e^2}{(\Gamma_{\rm in}^{-1} + \Gamma_{\rm out}^{-1})\left[\omega^2 + (\Gamma_{\rm in} + \Gamma_{\rm out})^2\right]}. \tag{20}$$

The cutoff frequency is determined by the total tunnelling rate $\Gamma \equiv \Gamma_{\rm in} + \Gamma_{\rm out}$, while the low(zero)-frequency magnitude is given by $4e^2/(\Gamma_{\rm in}^{-1} + \Gamma_{\rm out}^{-1})\Gamma^2$. Therefore, in principle, one can determine $\Gamma_{\rm in}$ and $\Gamma_{\rm out}$ from the power spectrum.

Figure 24(*a*) shows the power spectrum of the detector output, which is proportional to $S_q(\omega)$ [106]. The bottom curve, labelled CB, is measured when the upper QD is in the Coulomb blockade region, where no charge fluctuation is expected in the QD. This noise floor arises from a background charge fluctuation ($1/f$ spectrum) of the device in the low-frequency region ($\lesssim$1 kHz) and from white noise of the amplifier in the high-frequency region ($\gtrsim$1 kHz). When the QD is adjusted in the single-electron tunnelling regime, the excess power spectrum is observed as shown by curves #3–#6, in figure 24(*a*). The curves can be fitted

well with the Lorentzian profile (dashed line for #5), and the characteristic frequency (f_0) shifts in accordance with the gate voltage (corresponding to the tunnelling rate changing from ∼100 kHz (#3) to ∼10 Hz (#6)).

When a large bias voltage is applied, electrons transport from the left lead through the dot to the right lead ($\Gamma_{in} = \Gamma_L$ and $\Gamma_{out} = \Gamma_R$). This is the case where the average current is related to the charge fluctuation. Figure 24(*b*) shows typical real-time traces of the SET electrometer output. The histogram of the detector voltage is shown in figure 24(*c*). The trace measured in the single-electron tunnelling regime (#5) involves two-level fluctuations, as shown by the double-peak structure in the histogram. This contrasts with the other trace taken in the CB region (just noise with a single peak in the histogram). In the upper trace, represented by open circles for incoming and solid circles for outgoing processes, five electrons pass through the QD in a 10-ms period. The corresponding current (0.1 fA) is much smaller than the noise level of conventional current meters, which suggests possible application of the charge detection scheme for extremely sensitive current meter [100, 106, 107].

Real-time charge detection should work in the frequency range where the signal level is at least a couple of decibels higher than the noise level. As seen in the frequency spectrum (e.g. #5) of figure 24(*a*), the high-frequency limit is determined by the white noise of the measurement system, while the low-frequency limit is determined by $1/f$ noise of the device. The frequency range can be expanded by optimizing the device geometry to increase the coupling efficiency or by improving the measurement setup.

Single electron tunnelling is a correlated tunnelling process: an electron that has entered the small island leaves it before another electron is allowed to enter [59, 85]. Two-level fluctuations seen in the above measurement indeed originate from the single-electron tunnelling characteristics, excluding double occupancy. In addition, single-electron tunnelling provides intriguing time-correlated transport. In a one-dimensional array of small islands, Coulomb interaction (charge soliton) regulates the electron transport more periodically rather than random Poisson statistics [108]. Recently, a single peak in the frequency spectrum of charge fluctuation has been observed as a hallmark of single-electron tunnelling oscillation [109].

4.3. Single shot readout device for qubits

An important application of sensitive charge detection is a readout device for various kinds of qubits. It is desirable to determine a single qubit state with a reasonably high fidelity (single-shot readout). An important criterion for single-shot readout is that the measurement time (t_m) has to be much shorter than the dissipation time (T_1) of the qubit [110]. Since a back action on the qubit is inevitable, decoherence time (T_2) during the measurement process cannot exceed t_m. In order to minimize the influence during quantum computation, it is desirable to be able to switch on the measurement device only for the measurement process.

Naturally, charge measurement should be applied for readout of charge qubits [111]. Figure 25(*a*) shows a device structure containing a DQD in the upper electrical channel and a PC charge detector in the lower channel (The dotted regions are the conductive regions). The two channels are well isolated ($\gg$10 GΩ) by applying sufficiently large voltage V_{iso} to the isolation gate. The PC electrometer is placed on the left side of the structure so that the electrometer is more sensitive to the left dot and less sensitive to the right one. Thus, one electrometer is sufficient for detecting arbitrary charge states in the DQD.

First, we investigate a strongly (coherently) coupled DQD by conventional conductance measurement on the PC electrometer. The PC conductance is adjusted at the maximal sensitivity condition (about half the quantized conductance). In order to improve the signal-to-noise ratio, the charge state of the DQD is modulated by applying low-frequency (100 Hz)

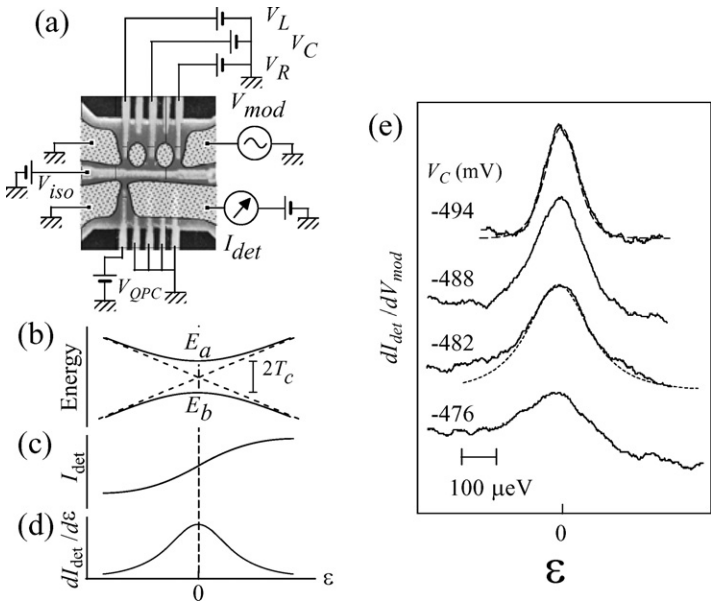

Figure 25. (*a*) Schematic measurement setup and a scanning electron micrograph of a double quantum dot coupled with a QPC electrometer. (*b*) Schematic energy diagram of eigenstates. (*c*) Current through the QPC. (*d*) The derivative of the QPC current. (*e*) Experimental charge detection signal. The dashed and dotted lines are fitted to the data by assuming thermal distribution and coherent tunnelling coupling, respectively.

sinusoidal voltage $V_{\rm mod}$ to the electrode as shown in figure 25(*a*), and the corresponding modulated current $I_{\rm det}$ through the PC is measured with a lock-in amplifier.

Figure 25(*b*) shows a schematic energy diagram of eigenenergies E_a and E_b when the energy bias ε (same definition as in section 2.1) is changed. The PC current should follow the charge occupation, $I_{\rm det} \sim |\langle R|\varphi\rangle|^2 - |\langle L|\varphi\rangle|^2$, as schematically shown for the bonding state in figure 25(*c*). The derivative curve, $\mathrm{d}I_{\rm det}/d\varepsilon$, is shown in figure 25(*d*) and is given by

$$\frac{\mathrm{d}I_{\rm det}}{\mathrm{d}\varepsilon} \sim \frac{\hbar^2 T_{\rm C}^2}{(\hbar^2 T_{\rm c}^2 + \varepsilon^2)^{3/2}}. \tag{21}$$

Figure 25(*e*) shows experimental traces of $\mathrm{d}I_{\rm det}/\mathrm{d}V_{\rm mod}$ around the charge degeneracy point $\varepsilon \equiv E_{\rm L} - E_{\rm R} = 0$. The energy scale in the figure was determined from photon assisted tunnelling spectroscopy with microwave irradiation (not shown) [19]. The peak in the topmost trace at the central gate voltage, $V_{\rm C} = -494\,\mathrm{mV}$, is the narrowest one observed in this measurement. The peak width is probably related to the external noise or ac modulation voltage used. The profile can be fitted well by assuming Fermi-Dirac distribution of charges (dashed line),

$$\frac{\mathrm{d}I_{\rm det}}{d\varepsilon} \sim \cosh^{-2}(\varepsilon/k_{\rm B}T_{\rm eff}), \tag{22}$$

with the effective thermal energy of $k_{\rm B}T_{\rm eff} \sim 30\,\mu\mathrm{eV}$ as a parameter. As the central gate voltage $V_{\rm C}$ is made less negative to increase the tunnelling coupling, the peak broadens, suggesting that the two QDs are coherently coupled by the tunnelling coupling. The peaks for the lowest two traces in figure 25(*e*) can be fitted well with equation 21 (see the dotted line fitted with $\hbar T_{\rm c} \sim 60\,\mu\mathrm{eV}$ for $V_{\rm C} = -482\,\mathrm{mV}$). The disagreement on the left-hand side arose from the

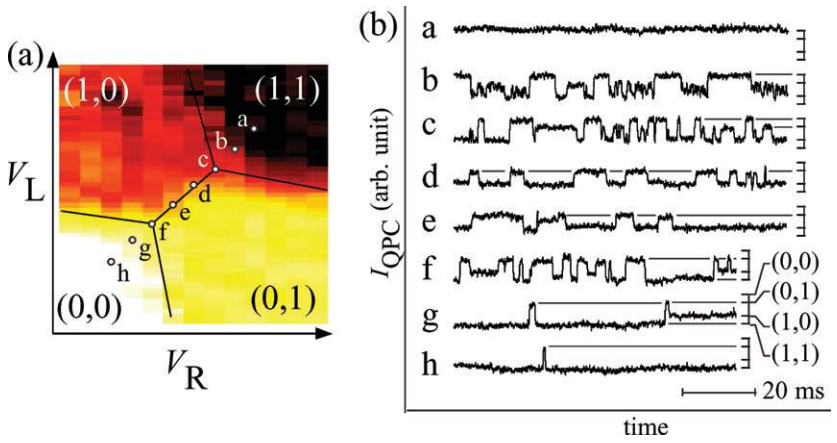

Figure 26. (*a*) PC charge detection of a DQD. The PC current (colour) is plotted as a function of two gate voltages V_L and V_R. Schematic charging diagram is attached. (*b*) Real time detection of charge fluctuation measured at several points a–h in (*a*).

broad positive signal from another peak on the left. Therefore, the experiment demonstrates that the PC detector can determine the charge distribution in a DQD even when the system is in a bonding state of the two localized charge states [112].

In contrast, when the DQD is weakly (incoherently) coupled, we can resolve time-dependent fluctuation between localized charge states. Figure 26(*a*) shows a charging diagram of the DQD obtained from the PC current profile (colour plot) when gate voltages V_L and V_R for the DQD are swept. When these gate voltages are fixed at several points (labelled a–h) in the diagram, we see charge fluctuation between some charge states as shown in figure 26(*b*). Three-level fluctuation is observed at points c and f, where three charge states are energetically degenerated, while two-level fluctuation is seen at d and e, where two charge states are degenerated. No significant fluctuation is observed at a and h, where the DQD is Coulomb blockaded. Observation of these fluctuations suggests the readout of the instantaneous charge state of a DQD, which is an encouraging single-shot readout. In this setup, charge states can be measured with a time resolution of about 500 μs.

However, there is a large gap between the measurement time and the typical T_1 ($\sim$10 ns, discussed in section 2.3) of the charge qubit in a DQD. This gap can be overcome by introducing an auxiliary island that traps an electron for a sufficiently long time for reading, as demonstrated for a superconducting charge qubit [25]. Another strategy is to make T_1 sufficiently long only during the measurement period. Since T_1 is determined by phonon emission process between the charge states, one can control its rate by changing the tunnelling barrier [113,114]. Therefore, single-shot readout for a charge qubit is feasible by switching the interdot coupling from the strong regime for coherent control to the weak regime for readout.

The electron spin state in a QD can also be measured with a charge detector by converting spin information to a charge state [36, 115]. Figure 27 illustrates spin-up and spin-down sublevels of a ground state of a one-electron QD connected to a lead. By adjusting the chemical potential of the lead between the Zeeman split sublevels in a magnetic field as shown in figure 27(*c*), only a spin-down electron (for negative g-factor material) is allowed to escape from the QD, and subsequently a spin-up electron is injected from the lead (figure 27(*d*)). Thus, single-spin measurement can be performed with an electrometer. The measurement has been demonstrated by applying a two-level voltage pulse to a gate electrode to empty the QD

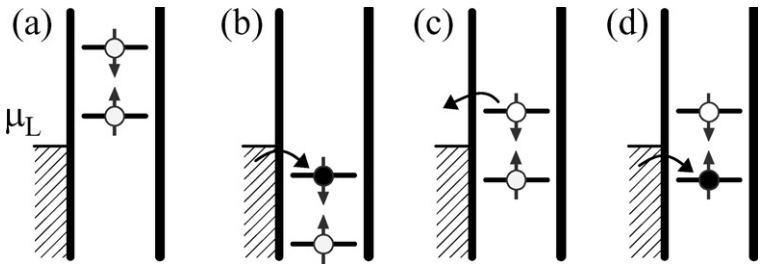

Figure 27. Schematic charging diagram for single-shot charge detection. (*a*) Emptying a quantum dot. (*b*) Injection of an electron with random spin orientation. The figure illustrates the case when spin-down electron is injected. (*c*) Reading out spin-down state. (*d*) Relaxing into spin-up ground state.

(figure 27(*a*)), inject an electron with random spin orientation (figure 27(*b*) for spin-down case) and read out the spin state (figures 27(*c*) and (*d*)). The charge state of the QD is measured with a PC electrometer. Since the pulse also changes the PC current, the current displays the charge state superimposed on the pulse waveform. The appearance of a signal in the read-out sequence indicates that a spin-down electron was injected into the QD. Measurement error arises from finite noise and limited bandwidth in the current measurement. The demonstration yields 65% visibility, which is high enough to say that a single-shot readout of an electron spin qubit has succeeded [36].

5. Summary

We have reviewed some time-dependent phenomena in semiconductor quantum dots. In the experiments shown in section 2, a high-speed voltage pulse is applied to induce coherent oscillations of a charge qubit in a double quantum dot. Tailoring the pulse waveform provides arbitrary unitary transformation in the one-qubit space. However, coupling to the environment causes decoherence (dissipation) problem. Although some decoherence mechanisms can be reduced by developing better fabrication techniques and refining measurement conditions, intrinsic electron–phonon interaction, especially piezoelectric coupling, would dominate the dissipation processes in semiconductors. In this sense, quantum dots in non-polar semiconductors (Si, carbon based material) may be preferable. Relaxation dynamics has also been focused in section 3, where the electronic pump–probe technique is used to determine the dissipation time. One can significantly reduce the relaxation rate by making use of spin selection rules for the relaxation. The spin degree of freedom is more isolated from the phonon bath, as we demonstrated in a quantum dot. This evidence has motivated many people to consider electron spin qubit as one of the best candidates for many-qubit systems. We have also discussed the spin selection rule for spin–orbit coupling in the two-electron system, in which the spin-correlated triplet state is expected to have a much longer relaxation time. A full understanding of the dissipation and decoherence mechanism may provide a clever way to overcome the decoherence problem. Moreover, the selection rule in the spin–orbit coupling can be used to create or determine spin entanglement state by combining with the charge detection scheme.

On the other hand, high-speed and high-precision measurement of a quantum state is desired to obtain a reliable outcome from a single qubit. In section 4, charge detection measurements with a single electron transistor or a quantum point contact device were described in the context of single-shot readout for charge and spin qubit. The technique is rapidly

developing for better visibility and higher speed. Interaction of a qubit with a measurement apparatus, which is one of the fundamental problems in quantum mechanics, can be investigated and designed in further studies. Moreover, charge detection scheme is expected to provide a single-electron counting device, in which individual electron tunnelling processes are recorded in a real time scale. Electron counting statistics will be a new tool to investigate correlated electron transport of a small current.

Finally, these techniques can be combined with other mesoscopic electron devices, such as electron interferometer and beam splitter, by means of nanotechnology. In analogy with the optical technique used in quantum optics, integration of these components would provide a novel measurement concept for nontrivial quantum states. We believe these techniques can be applied for a better understanding of quantum transport in nanostructures as well as for developing quantum engineering in solid state devices.

Acknowledgments

We thank T Brandes, Y Hirayama, T Itakura, Y Nakamura, S Tarucha, and Y Tokura for stimulating discussions. Some of the presented works were supported by the Strategic Information and Communications R&D Promotion Programme (SCOPE) of the Ministry of Internal Affairs and Communications of Japan, Grant-in-Aid for Scientific Research from the Japan Society for the Promotion of Science and Solution Oriented Research for Science and Technology (SORST Program) of the Japan Science and Technology Agency.

References

[1] Nielsen M A and Chuang I L 2000 *Quantum Computation and Quantum Information* (Cambridge: Cambridge University Press)
[2] Bouwmeester D, Ekert A and Zeilinger A (ed) 2000 *The Physics of Quantum Information* (Berlin: Springer)
[3] Vandersypen L M K, Steffen M, Breyta G, Yannoni C S, Sherwood M H and Chuang I L 2001 Experimental realization of Shor's quantum factoring algorithm using nuclear magnetic resonance *Nature* **414** 883
[4] Nakamura Y, Pashkin Yu A and Tsai J S 1999 Coherent control of macroscopic quantum states in a single-Cooper-pair box *Nature* **398** 786
[5] Chiorescu I, Bertet P, Semba K, Nakamura Y, Harmans C J P M and Mooij J E 2004 Coherent dynamics of a flux qubit coupled to a harmonic oscillator *Nature* **431** 159
[6] Wallraff A, Schuster D I, Blais A, Frunzio L, Huang R-S, Majer J, Kumar S, Girvin S M and Schoelkopf R J 2004 Strong coupling of a single photon to a superconducting qubit using circuit quantum electrodynamics *Nature* **431** 162
[7] Kamada H, Gotoh H, Temmyo J, Takagahara T and Ando H 2001 Exciton Rabi oscillation in a single quantum dot *Phys. Rev. Lett.* **87** 246401
[8] Jelezko F, Gaebel T, Popa I, Domhan M, Gruber A and Wrachtrup J 2004 Observation of coherent oscillation of a single nuclear spin and realization of a two-qubit conditional quantum gate *Phys. Rev. Lett.* **93** 130501
[9] Yusa G, Muraki K, Takashina K, Hashimoto K and Hirayama Y 2005 Controlled multiple quantum coherences of nuclear spins in a nanometre-scale device *Nature* **434** 1001
[10] Weiss U 2001 *Quantum Dissipative Systems* (Singapore: World Scientific)
[11] DiVincenzo D P 1997 *Mesocopic Electron Transport* (*NATO ASI Series E* 345) ed L L Sohn *et al* (Dordrecht: Kluwer) pp 657–77
[12] Nakamura Y, Pashkin Yu A, Yamamoto T and Tsai J S 2002 Charge echo in a cooper-pair box *Phys. Rev. Lett.* **88** 047901
[13] Vion D, Aassime A, Cottet A, Joyez P, Pothier H, Urbina C, Esteve D and Devoret M H 2002 Manipulating the quantum state of an electrical circuit *Science* **296** 886
[14] Kouwenhoven L P, Marcus C M, McEuen P L, Tarucha S, Westervelt R M and Wingreen N S 1997 *Mesoscopic Electron Transport* (*NATO ASI Series E* 345) ed Sohn L L *et al* (Dordrecht: Kluwer) pp 105–214
[15] Kouwenhoven L P, Austing D G and Tarucha S 2001 Few-electron quantum dots *Rep. Prog. Phys.* **64** 701

[16] Tarucha S, Austing D G, Honda T, van der Hage R J and Kouwenhoven L P 1996 Shell filling and spin effects in a few electron quantum dot *Phys. Rev. Lett.* **77** 3613
[17] Kouwenhoven L P, Oosterkamp T H, Danoesastro M W S, Eto M, Austing D G, Honda T and Tarucha S 1997 Excitation spectra of circular, few-electron quantum dots *Science* **278** 1788
[18] Hayashi T, Fujisawa T, Cheong H D and Hirayama Y 2003 Coherent manipulation of electronic states in a double quantum dot *Phys. Rev. Lett.* **91** 226804
[19] Oosterkamp T H, Fujisawa T, van der Wiel W G, Ishibashi K, Hijman R V, Tarucha S and Kouwenhoven L P 1998 Microwave spectroscopy of a quantum-dot molecule *Nature* **395** 873
[20] Fujisawa T, Hayashi T, Cheong H D, Jeong Y H and Hirayama Y 2004 Rotation and phase-shift operations for a charge qubit in a double quantum dot *Physica* E **21** 1046
[21] Fujisawa T, Hayashi T and Hirayama Y 2004 Controlled decoherence of a charge qubit in a double quantum dot *J. Vac. Sci. Technol.* B **22** 2035
[22] Barenco A, Deutsch D, Ekert A and Jozsa R 1995 Conditional quantum dynamics and logic gates *Phys. Rev. Lett.* **74** 4083
[23] Fedichkin L, Yanchenko M and Valiev K A 2000 Coherent charge qubits based on GaAs quantum dots with a built-in barrier *Nanotechnology* **11** 387
[24] Yamamoto T, Pashkin Yu A, Astafiev O, Nakamura Y and Tsai J S 2003 Demonstration of conditional gate operation using superconducting charge qubits *Nature* **425** 941
[25] Astafiev O, Pashkin Yu A, Nakamura Y, Yamamoto T and Tsai J S 2004 Quantum noise in the Josephson charge qubit *Phys. Rev. Lett.* **93** 267007
[26] Kirton M J and Uren M J 1989 Noise in solid-state microstructures—a new perspective on individual defects, interface states and low-frequency $(1/f)$ noise *Adv. Phys.* **38** 367
[27] Brandes T and Kramer B 1999 Spontaneous emission of phonons by coupled quantum dots *Phys. Rev. Lett.* **83** 3021
[28] Brandes T and Vorrath T 2002 Adiabatic transfer of electrons in coupled quantum dots *Phys. Rev.* B **66** 075341
[29] Fujisawa T, Oosterkamp T H, van der Wiel W G, Broer B W, Aguado R, Tarucha S and Kouwenhoven L P 1998 Spontaneous emission spectrum in double quantum dot devices *Science* **282** 932
[30] Bandyopadhyay S and Roychowdhury V P 1997 Switching in a reversible spin logic gate *Superlatt. Microstruct.* **22** 411
[31] Loss D and DiVincenzo D P 1998 Quantum computation with quantum dots *Phys. Rev.* A **57** 120
[32] Burkard G, Loss D and DiVincenzo D P 1999 Coupled quantum dots as quantum gates *Phys. Rev.* B **59** 2070
[33] Hatano T, Stopa M and Tarucha S 2005 Single-electron delocalization in hybrid vertical-lateral double quantum dots *Science* **309** 268
[34] Hanson R, Witkamp B, Vandersypen L M K, Willems van Beveren L H, Elzerman J M and Kouwenhoven L P 2003 Zeeman energy and spin relaxation in a one-electron quantum dot *Phys. Rev. Lett.* **91** 196802
[35] Hanson R, Vandersypen L M K, Willems van Beveren L H, Elzerman J M, Vink I T and Kouwenhoven L P 2004 Semiconductor few-electron quantum dot operated as a bipolar spin filter *Phys. Rev.* B **70** 241304
[36] Elzerman J M, Hanson R, Willems van Beveren L H, Witkamp B, Vandersypen L M K and Kouwenhoven L P 2004 Single-shot read-out of an individual electron spin in a quantum dot *Nature* **430** 431
[37] Winkler R 2003 *Spin-Orbit Coupling Effects in Two-Dimensional Electron and Hole Systems* (Berlin: Springer)
[38] Frenkel D M 1991 Spin relaxation in GaAs/Al_xGa_{1-x}As heterostructures in high magnetic fields *Phys. Rev.* B **43** 14228
[39] Khaetskii A V and Nazarov Yu V 2000 Spin relaxation in semiconductor quantum dots *Phys. Rev.* B **61** 12639
[40] Kroutvar M, Ducommun Y, Heiss D, Bichler M, Schuh D, Abstreiter G and Finley J J 2004 Optically programmable electron spin memory using semiconductor quantum dots *Nature* **432** 81
[41] Fujisawa T, Austing D G, Tokura Y, Hirayama Y and Tarucha S 2002 Allowed and forbidden transitions in artificial hydrogen and helium atoms *Nature* **419** 278
[42] Koppens F H L, Folk J A, Elzerman J M, Hanson R, Willems van Beveren L H, Vink I T, Tranitz H P, Wegscheider W, Kouwenhoven L P and Vandersypen L M K 2005 Control and detection of singlet-triplet mixing in a random nuclear field *Science* **309** 1346
[43] Xiao M, Martin I, Yablonovitch E and Jiang H W 2004 Electrical detection of the spin resonance of a single electron in a silicon field-effect transistor *Nature* **430** 435
[44] Kato Y, Myers R C, Driscoll D C, Gossard A C, Levy J and Awschalom D D 2003 Gigahertz electron spin manipulation using voltage-controlled g-tensor modulation *Science* **299** 1201
[45] Tarucha S, Austing D G, Tokura Y, van der Wiel W G and Kouwenhoven L P 2000 Direct Coulomb and exchange interaction in artificial atoms *Phys. Rev. Lett.* **84** 2485
[46] Liu H W, Fujisawa T, Hayashi T and Hirayama Y 2005 Pauli spin blockade in cotunnelling transport through a double quantum dot *Phys. Rev.* B **72** 161305

[47] Petta J R, Johnson A C, Taylor J M, Laird E A, Yacoby A, Lukin M D, Marcus C M, Hanson M P and Gossard A C 2005 Coherent manipulation of coupled electron spins in semiconductor quantum dots *Science* **309** 2180
[48] Taylor J M, Marcus C M and Lukin M D 2003 Long-lived memory for mesoscopic quantum bits *Phys. Rev. Lett.* **90** 206803
[49] Beenakker C W J and van Houten H 1991 Quantum transport in semiconductor nanostructure *Solid State Phys. Adv. Res. Appl.* **44** 1
[50] Hirayama Y, Saku T, Tarucha S and Horikoshi Y 1991 Ballistic electron-transport in macroscopic 4-terminal square structures with high mobility *Appl. Phys. Lett.* **58** 2672
[51] Spector J, Stormer H L, Baldwin K W, Pfeiffer L N and West K W 1990 Refractive switch for 2 dimensional electrons *Appl. Phys. Lett.* **56** 2433
[52] Aharonov Y and Bohm D 1959 Significance of electromagnetic potentials in the quantum theory *Phys. Rev.* **115** 485
[53] Al'tshuler B L, Aronov A G and Spivak B Z 1981 The Aharonov-Bohm effect in disordered conductors *JETP Lett.* **33** 94
Al'tshuler B L, Aronov A G and Spivak B Z 1981 *Pis'ma Zh. Teor. Fiz.* **33** 101
[54] Timp G, Chang A M, DeVegvar P, Howard R E, Behringer R, Cunningham J E and Mankiewich P 1988 Quantum transport in one-dimensional GaAs/AlGaAs microstructures *Surf. Sci.* **196** 68
[55] Schuster R, Buks E, Heiblum M, Mahalu D, Umansky V and Shtrikman H 1997 Phase measurement in a quantum dot via a double-slit interference experiment *Nature* **385** 417
[56] Liu R C, Odom B, Yamamoto Y and Tarucha S 1998 Quantum interference in electron collision *Nature* **391** 263
[57] Recher P, Saraga D S and Loss D 2004 Creation and detection of mobile and non-local spin-entangled electrons *Preprint* cond-mat/0408526
[58] Beenakker C W J, DiVincenzo D P, Emary C and Kindermann M 2004 Charge detection enables free-electron quantum computation *Phys. Rev. Lett.* **93** 020501
[59] Grabert H and Devoret M H (ed) 1991 *Single Charge Tunneling, Coulomb Blockade Phenomena in Nanostuctures* (*NATO ASI Series B* 294) (New York: Plenum)
[60] van der Wiel W G, De Franceschi S, Elzerman J M, Fujisawa T, Tarucha S and Kouwenhoven L P 2003 Electron transport through double quantum dots *Rev. Mod. Phys.* **75** 1
[61] Waugh F R, Berry M J, Mar D J, Westervelt R M, Campman K L and Gossard A C 1995 Single-electron charging in double and triple quantum dots with tunable coupling *Phys. Rev. Lett.* **75** 705
[62] Livermore C, Crouch C H, Westervelt R M, Campman K L and Gossard A C 1996 The Coulomb blockade in coupled quantum dots *Science* **274** 1332
[63] Nazarov Yu V 1993 Quantum interference, tunnel-junctions and resonant-tunnelling interferometer *Physica* B **189** 57
[64] van der Vaart N C, Godijn S F, Nazarov Yu V, Harmans C J P M and Mooij J E 1995 Resonant-tunnelling through 2 discrete energy levels *Phys. Rev. Lett.* **74** 4702
[65] Fujisawa T and Tarucha S 1997 Photon assisted tunnelling in single and coupled quantum dot systems *Superlatt. Microstruct.* **21** 247
[66] Stoof T H and Nazarov Yu V 1996 Time-dependent resonant tunnelling via two discrete states *Phys. Rev.* B **53** 1050
[67] Stafford C A and Wingreen N S 1996 Resonant photon-assisted tunnelling through a double quantum dot: an electron pump from spatial rabi oscillations *Phys. Rev. Lett.* **76** 1916
[68] van der Wiel W G, Fujisawa T, Oosterkamp T H and Kouwenhoven L P 1999 Microwave spectroscopy of a double quantum dot in the low- and high-power regime *Physica* B **272** 31
[69] Itakura T and Tokura Y 2003 Dephasing due to background charge fluctuations *Phys. Rev.* B **67** 195320
[70] Paladino E, Faoro L, Falci G and Fazio R 2002 Decoherence and $1/f$ noise in Josephson qubits *Phys. Rev. Lett.* **88** 228304
[71] Jung S W, Fujisawa T, Hirayama Y and Jeong Y H 2004 Background charge fluctuation in a GaAs quantum dot device *Appl. Phys. Lett.* **85** 768
[72] Pioro-Ladrière M, Davies J H, Long A R, Sachrajda A S, Gaudreau L, Zawadzki P, Lapointe J, Gupta J, Wasilewski Z and Studenikin S A 2005 The origin of switching noise in GaAs/AlGaAs lateral gated devices *Preprint* cond-mat/0503602
[73] Eto M 2001 Electronic states and transport phenomena in quantum dot systems *Japan. J. Appl. Phys.* **40** 1929
[74] Seeger K 1985 *Semiconductor Physics: An Introduction* (Berlin: Springer) pp 153–213
[75] Hollenberg L C L, Dzurak A S, Wellard C, Hamilton A R, Reilly D J, Milburn G J and Clark R G 2004 Charge-based quantum computing using single donors in semiconductors *Phys. Rev.* B **69** 113301

[76] Brandes T, Renzoni F and Blick R H 2001 Adiabatic steering and determination of dephasing rates in double-dot qubits *Phys. Rev.* B **64** 035319
[77] Fujisawa T, Austing D G, Tokura Y, Hirayama Y and Tarucha S 2003 Electrical pulse measurement, inelastic relaxation and non-equilibrium transport in a quantum dot *J. Phys.: Condens. Matter. (Topical Review)* **15** R1395
[78] Fujisawa T, Tokura Y and Hirayama Y 2001 Transient current spectroscopy of a quantum dot in the Coulomb blockade regime *Phys. Rev.* B **63** 081304(R)
[79] Fujisawa T, Tokura Y and Hirayama Y 2001 Energy relaxation process in a quantum dot studied by DC current and pulse-excited current measurements *Physica* B **298** 573
[80] Tokura Y, Sasaki S, Austing D G and Tarucha S 2001 Excitation spectra and exchange interactions in circular and elliptical quantum dots *Physica* B **298** 260–4
[81] Benisty H 1995 Reduced electron–phonon relaxation rates in quantum-box systems—theoretical analysis *Phys. Rev.* B **51** 13281
[82] Weinmann D, Häusler W and Kramer B 1995 Spin blockades in linear and nonlinear transport through quantum dots *Phys. Rev. Lett.* **74** 984
[83] Bockelmann U and Bastard G 1990 Phonon-scattering and energy relaxation in 2-dimemsional, one-dimensional and zero-dimensional electron gases *Phys. Rev.* B **42** 8947
[84] Bockelmann U 1994 Phonon-scattering between zero-dimensional electronic states—spatial versus Launau *Phys. Rev.* B **50** 17271
[85] Fujisawa T, Austing D G, Tokura Y, Hirayama Y and Tarucha S 2002 Nonequilibrium transport through a vertical quantum dot in the absence of spin-flip energy relaxation *Phys. Rev. Lett.* **88** 236802
[86] Fujisawa T, Tokura Y, Austing D G, Hirayama Y and Tarucha S 2002 Spin-dependent energy relaxation inside a quantum dot *Physica* B **314** 224
[87] De Franceschi S, Sasaki S, Elzerman J M, van der Wiel W G, Tarucha S and Kouwenhoven L P 2001 Electron cotunnelling in a semiconductor quantum dot *Phys. Rev. Lett.* **86** 878
[88] Averin D V and Nazarov Yu V 1991 *Single Charge Tunneling, Coulomb Blockade Phenomena in Nanostuctures* (*NATO ASI Series B* 294) ed H Grabert and M H Devoret (New York: Plenum) pp 217–48
[89] Sachrajda A S *et al* 2001 Spin polarized injection into a quantum dot by means of the spatial separation of spins *Physica* E *(Amsterdam)* **10** 493
[90] Ciorga M *et al* 2001 Readout of a single electron spin based quantum bit by current detection *Physica* E *(Amsterdam)* **11** 35
[91] Khaetskii A V and Nazarov Yu V 2000 Spin-dephasing processes in semiconductor quantum dots *Physica* E **6** 470
[92] Bulaev D V and Loss D 2005 Spin relaxation and anticrossing in quantum dots: Rashba versus Dresselhaus spin-orbit coupling *Phys. Rev.* B **71** 205324
[93] Dickmann S and Hawrylak P 2003 Spin-singlet-spin-triplet transitions in quantum dots *J. Supercond.* **16** 387
[94] Drouvelis P S *et al* 2004 Effects of anisotropy and magnetic fields on two-electron parabolic quantum dots *J. Phys.: Condens. Matter.* **16** 3633
[95] Maksym P A 1998 Quantum states of interacting electrons in a 2D elliptical quantum dot *Physica* B *(Amsterdam)* **249–251** 233
[96] Ono K and Tarucha S 2004 Nuclear-spin-induced oscillatory current in spin-blockaded quantum dots *Phys. Rev. Lett.* **92** 256803
[97] Ono K, Austing D G, Tokura Y and Tarucha S 2002 Current rectification by Pauli exclusion in a weakly coupled double quantum dot system *Science* **297** 1313
[98] Devoret M H and Schoelkopf R J 2000 Amplifying quantum signals with the single-electron transistor *Nature* **406** 1039
[99] Korotkov A N and Paalanen M A 1999 Charge sensitivity of radio frequency single-electron transistor *Appl. Phys. Lett.* **74** 4052
[100] Schoelkopf R J, Wahlgren P, Kozhevnikov A A, Delsing P and Prober D E 1998 The radio-frequency single-electron transistor (RF-SET): a fast and ultrasensitive electrometer *Science* **280** 1238
[101] Fujisawa T and Hirayama Y 2000 Charge noise analysis of an AlGaAs/GaAs quantum dot using transmission-type radio-frequency single-electron transistor technique *Appl. Phys. Lett.* **77** 543
[102] van Wees B J, Kouwenhoven L P, van Houten H, Beenakker C W J, Mooij J E, Foxon C T and Harris J J 1988 Quantized conductance of magnetoelectric subbands in ballistic point contacts *Phys. Rev.* B **38** 3625
[103] Field M, Smith C G, Pepper M, Ritchie D A, Frost J E F, Jones G A C and Hasko D G 1993 Measurements of Coulomb blockade with a noninvasive voltage probe *Phys. Rev. Lett.* **70** 1311
[104] Rushforth A W, Smith C G, Godfrey M D, Beere H E, Ritchie D A and Pepper M 2004 Noninvasive detection of the evolution of the charge states of a double dot system *Phys. Rev.* B **69** 113309

[105] Cheong H D, Fujisawa T, Hayashi T, Hirayama Y and Jeong Y H 2002 Impedance analysis of a radio-frequency single-electron transistor *Appl. Phys. Lett.* **81** 3257
[106] Fujisawa T, Hayashi T, Hirayama Y, Cheong H D and Jeong Y H 2004 Electron counting of single-electron tunnelling current *Appl. Phys. Lett.* **84** 2343
[107] Lu W, Ji Z, Pfeiffer L, West K W and Rimberg A J 2003 Real-time detection of electron tunnelling in a quantum dot *Nature* **423** 422
[108] Delsing P, Likharev K K, Kuzmin L S and Claeson T 1989 Time-correlated single-electron tunnelling in one-dimensional arrays of ultrasmall tunnel-junctions *Phys. Rev. Lett.* **63** 1861
[109] Bylander J, Duty T and Delsing P 2005 Current measurement by real-time counting of single electrons *Nature* **434** 361
[110] Makhlin Yu, Schön G and Shnirman A 2000 Statistics and noise in a quantum measurement process *Phys. Rev. Lett.* **85** 4578 (2000)
[111] Aassime A, Johansson G, Wendin G, Schoelkopf R J and Delsing P 2001 Radio-frequency single-electron transistor as readout device for qubits: charge sensitivity and backaction *Phys. Rev. Lett.* **86** 3376
[112] DiCarlo L, Lynch H J, Johnson A C, Childress L I, Crockett K, Marcus C M, Hanson M P and Gossard A C 2004 Differential charge sensing and charge delocalization in a tunable double quantum dot *Phys. Rev. Lett.* **92** 226801
[113] Fujisawa T, van der Wiel W G and Kouwenhoven L P 2000 Inelastic tunnelling in a double quantum dot coupled to a bosonic environment *Physica* E **7** 413
[114] Hayashi T, Fujisawa T, Tomita R and Hirayama Y Real-time observation of charge states and energy relaxation in a double quantum dot *Japan. J. Appl. Phys.* at press
[115] Kane B E, McAlpine N S, Dzurak A S, Clark R G, Milburn G J, Sun H B and Wiseman H 2000 Single-spin measurement using single-electron transistors to probe two-electron systems *Phys. Rev.* B **61** 2961